

1 **Large and primarily updip afterslip following the 2012  $M_w$  7.6 Nicoya, Costa Rica**  
2 **earthquake**

3 **AUTHORS:** <sup>1</sup>Hobbs, T.E., <sup>2</sup>Kyriakopoulos, C., <sup>1</sup>Newman, A.V., <sup>3</sup>Protti, M., <sup>1</sup>Yao, D.

4 Accepted 27/06/2017 J. Geophys. Res. (doi:/10.1002/2017JB014035)

5 **AUTHOR AFFILIATIONS**

6 <sup>1</sup>School of Earth and Atmospheric Sciences, Georgia Institute of Technology, 311 Ferst  
7 Dr, Atlanta, GA, USA, 30332

8 <sup>2</sup>Department of Earth Sciences, University of California, Riverside, 900 University Av.,  
9 Riverside, CA, USA, 92521

10 <sup>3</sup>Observatorio Vulcanológico y Sismológico de Costa Rica, PO Box 2386-3000, Heredia,  
11 Costa Rica

12  
13 **KEY POINTS**

- 14 • Postseismic deformation is recorded for 3.5 years following the 2012  $M_w$  7.6  
15 Nicoya earthquake in Costa Rica
- 16 • Up to 1.7 m of afterslip is observed at the periphery of coseismic slip and near the  
17 Gulf of Nicoya
- 18 • Afterslip and aftershocks appear to be anticorrelated and potentially linked to fault  
19 properties or subducted structures

20  
21 **ABSTRACT**

22 We present detailed surface measurements of the first 3.5 years of postseismic  
23 deformation following the 5 September 2012 moment magnitude ( $M_w$ ) 7.6 Nicoya, Costa  
24 Rica earthquake. The dominant signal in the first 2.5 years is uniform horizontal  
25 trenchward motion totaling 7-26 cm across 40 stations. Trenchward velocity is strongly  
26 diminished by mid 2014 and appears by 2016 to have begun reversing. We invert the first  
27 2.5 years to determine the corresponding afterslip on a detailed 3D interface. Results  
28 show significant afterslip both up and down dip of the main coseismic rupture zone, with  
29 as much as 1.7 m of offset in two patches at 15-20 km depth and immediately up-dip of  
30 the maximum coseismic slip. This updip slip represents an important mechanism to  
31 address unrelieved interseismic locking, although sufficient strain energy remains to  
32 generate up to a  $M_w$  7.1 event near the coastline. The afterslip patches are anticorrelated  
33 with strongly-clustered aftershocks at the same depth, which is indicative of varying  
34 frictional behavior along strike. An additional patch of slip is collocated with reoccurring  
35 slow slip events beneath the Gulf of Nicoya. The magnitude of the observed slip,  
36 however, cannot be sufficiently explained by the known slow-slip events. Ongoing  
37 measurements will be crucial to understanding the relocking process in Nicoya.

38  
39 **INDEX TERMS:** 8104 Continental margins: convergent; 8118 Dynamics and  
40 mechanics of faulting; 8158 Plate motions: present and recent; 7230 Seismicity and  
41 tectonics; 7240 Subduction zones

42  
43 **KEYWORDS:** Postseismic, afterslip, aftershocks, fault friction

## 44 1 INTRODUCTION

45 In the quest to understand the seismic cycle, much attention is paid to coseismic  
46 motions and their potential precursors. While often less destructive, postseismic  
47 processes largely control deformation in the years to decades following a large  
48 earthquake [e.g. Khazaradze et al., 2002; Hu et al., 2004; Wang et al., 2012]. Postseismic  
49 motion results from the combined effects of: afterslip, the aseismic continuation of  
50 coseismic motion; poroelastic relaxation, short-lived deformation related to postseismic  
51 porefluid flow; viscoelastic relaxation, the long term inelastic response of the mantle to  
52 coseismic stress; and relocking, the return to more stable interseismic accumulation of  
53 strain energy [Wang et al., 2012]. Accounting for these processes is crucial to accurately  
54 estimate the accumulation of stress at later stages of the seismic cycle, that in turn  
55 improve assessments for earthquake and tsunami potential. To be reliable, postseismic  
56 deformation measurements require techniques sensitive enough to record small changes  
57 in position over years to decades that span an area of several thousand square kilometers  
58 or more. This is unavailable in the majority of subduction zones, where the seismogenic  
59 portion of the fault exists offshore and/or where funding prohibits operation of a  
60 temporally and spatially dense network.

61 Figure 1 highlights why the Nicoya Peninsula is particularly well situated to study  
62 a myriad of subduction zone processes. The Nicoya Peninsula sits immediately above the  
63 seismogenic zone and extends to within 60 km of the trench, allowing measurements of  
64 crustal motions to be taken from much closer to their source regions than would be  
65 possible in most other areas. As a result of this land geometry, Nicoya has been the focus  
66 of numerous geophysical investigations over the past 20 years. Previous studies have  
67 utilized seismic [e.g. Newman et al., 2002; DeShon et al., 2006; Dinc et al., 2010] and  
68 geodetic networks [e.g. LaFemina et al., 2009; Feng et al., 2012; Dixon et al., 2014],  
69 ocean drilling [e.g. Vannucchi et al., 2001; Davis et al., 2015], heat flow measurements  
70 [e.g. Harris & Wang, 2002; Harris et al., 2010], and geomorphological observations [e.g.  
71 Marshall & Anderson, 1995; Sak et al., 2009; Protti et al., 2014] to characterize the  
72 megathrust in detail.

73 Convergence of the Cocos and Caribbean plates is sufficiently rapid to generate  
74  $M \geq 7$  earthquakes beneath the peninsula roughly every 50 years since 1853 [Protti et al.,  
75 1995; Feng et al., 2012]. In addition to these larger earthquakes, the Nicoya megathrust  
76 exhibits persistent tremor activity and very low frequency microseismicity up- and  
77 downdip of the seismogenic zone [Walter et al., 2011; Walter et al., 2013]. The low  
78 frequency earthquakes and tremor are sometimes coincident with slow slip events  
79 occurring about once a year between 2007 and 2012 [Outerbridge et al., 2010; Jiang et  
80 al., 2012; Dixon et al., 2014]. This measurable complexity of fault behavior has  
81 established Nicoya as a rich natural laboratory for subduction zone studies (see  
82 <http://nicoya.eas.gatech.edu> for more information).

83 The most recent large earthquake was the 5 September 2012 moment magnitude  
84 ( $M_w$ ) 7.6 Nicoya earthquake (Figure 1), which was preceded by a 9-day foreshock  
85 sequence [Walter et al., 2015]. This event nucleated 10 km offshore at 13 km depth along  
86 the interface [Yue et al., 2013], with rupture concentrating downdip and beneath the  
87 peninsula [Yue et al., 2013; Protti et al., 2014; Liu et al., 2015; Kyriakopoulos &  
88 Newman, 2016]. The approximately 110 by 50 km coseismic rupture area [Liu et al.,  
89 2015] is shown by Protti et al. [2014] to roughly align with the region of significant ( $\geq$

90 50%) previous interseismic locking [Feng et al., 2012]. A potential zone of unreleased  
91 slip in the Protti et al. [2014] model, located immediately offshore and north west of the  
92 hypocenter [Figure 4b in Protti et al., 2014], was shown by Kyriakopoulos and Newman  
93 [2016] to be partially diminished in amplitude and spatial extent when a fully 3D slab  
94 geometry is implemented. It is expected that postseismic slip will release much of this  
95 remaining strain energy, effectively balancing the slip budget before Nicoya enters a new  
96 seismic cycle.

97 Here we use a novel dataset of campaign and continuous land-based global  
98 positioning system (GPS) observations on and near the Nicoya Peninsula to measure  
99 ongoing postseismic deformation from 2012 to 2016. These data directly record the  
100 timing and spatial extent of surface deformation from the combined postseismic  
101 processes. Geodetic inversions are carried out and compared spatially against inter- and  
102 coseismic fault slip, aftershocks, and cumulative slow slip to establish the contribution of  
103 postseismic phenomena to the seismic cycle budget. Insights from well-instrumented  
104 locations like Nicoya are critical to understanding seismic cycle behavior in subduction  
105 zones like Cascadia [Wang & Tréhu, 2016], which have relatively sparse near-trench  
106 coverage. In coming years, we expect to record accelerating landward motion as the  
107 subduction zone re-enters an interseismic state.

## 108 **2 METHODS**

### 109 **2.1 Data Collection**

110 Following a post-earthquake deployment in 2012, field work was again completed  
111 in March 2015 and 2016 on the Nicoya Peninsula to obtain new campaign GPS data. By  
112 returning to these sites at the same time each year we minimize most seasonal variations  
113 that could otherwise affect GPS calculations. In the field campaign from March 6-19,  
114 2015, GPS data were collected at 31 stations on and around the Nicoya Peninsula and  
115 Arenal volcano, with instruments recording continuously for 2-3 days at a 30 second  
116 sampling interval. Of interest to this study is the subset of 22 stations for which there are  
117 previous campaign data taken in 2012 right after the earthquake (Figure 2a, details  
118 provided in Table 1 and 2). Post-processing of the raw data is completed using the precise  
119 point positioning software “GIPSY-OASIS”, made available by the Jet Propulsion  
120 Laboratory (JPL). Final fiducial-free daily solutions are determined using precise satellite  
121 orbits provided by JPL and ocean loading coefficients from the FES2004 hydrodynamic  
122 model [Letellier, 2005], with ambiguity resolution handled by AMBIZAP [Blewitt,  
123 2008]. March 2016 measurements followed the same procedure for a subset of 7  
124 campaign sites in the central peninsula, focusing on stations with poorer coverage during  
125 the 2015 campaign (Figure 2b).

126 These data follow the most recent prior campaign conducted in 2012, in rapid  
127 response to the 5 September 2012 Nicoya earthquake [Protti et al., 2014]. Instruments  
128 were deployed between September 8-22, 2012, with all units recording a minimum of 3  
129 complete Coordinated Universal Time (UTC) days. Several stations (COBA, DIRI,  
130 GUIO, MATA, and MIRM) were left in continuous mode to measure several consecutive  
131 months of postseismic deformation.

132 In addition to campaign measurements, data were also collected from a network  
133 of 18 continuously recording GPS stations on and near the Nicoya Peninsula. This  
134 network is operated by the University of South Florida (USF) and the Observatorio  
135

136 Vulcanológico y Sismológico de Costa Rica (OVSICORI), with technical support from  
137 UNAVCO (<http://www.unavco.org>) (Tables 1 and 2). Shown in Figure 3, time series of  
138 daily position solutions are created for a subset of continuous GPS station daily solutions  
139 for which there was good temporal coverage. It is immediately evident that there is a  
140 strongly non-linear displacement in the first several months, which flattens out at most  
141 stations by approximately 2014. By the start of 2015 most stations appear to show a  
142 gentle reversal in direction of their initial post-seismic motion, continuing until at least  
143 the end of the time series (31 May 2016).

144 Due to the sparsity of the data points for campaign measurements, non-linear  
145 postseismic velocities cannot be well-constrained at each site. Instead, cumulative offsets  
146 are computed at all 40 stations by differencing start and end positions for the time  
147 periods: 2.5 years from immediately following the earthquake to March 2015, and 1 year  
148 from March 2015 to March 2016 (to match timing of campaign measurements). Only  
149 daily positions with formal horizontal error of less than 1 cm are used in calculating  
150 displacement. Earliest postseismic positions are taken as the average position over the  
151 first 2 days of available post-seismic recordings, corresponding to the date used in Protti  
152 et al. [2014] to define the end of coseismic displacement. For the 2015 and 2016  
153 campaigns we average over all available days, up to 4. Continuous datasets are sampled  
154 using a 4-day window corresponding to the average timing of the campaign  
155 measurements. The start period of 2 days was chosen to retain as much of the early  
156 postseismic signal as possible. Displacements at each station were converted from  
157 ITRF2008 reference frame [Altamimi et al., 2011], to a stable Caribbean plate using  
158 DeMets et al. [2010]. Beginning and end times, as well as displacements for each station  
159 are given in Table 1 for 2012-2015 and Table 2 for 2015-2016.

160 As we do not capture the first hours to days of afterslip, measurements herein are  
161 a lower bound on total afterslip, emphasizing the spatial distribution of slip over the  
162 course of several years. However, our 2012 ‘start’ date reflects the ‘end’ date of previous  
163 coseismic geodetic studies [Protti et al., 2014; Kyriakopoulos & Newman, 2016],  
164 allowing for direct comparison between those results and our observed postseismic  
165 deformation. For a discussion of earliest afterslip from high-rate GPS please see  
166 Malservisi et al., [2015]. While we do not account for aftershocks independently, their  
167 contribution to total slip is included in and discussed in our results.

168

## 169 **2.2 Afterslip Inversion**

170 To quantify the subsurface processes responsible for postseismic displacements,  
171 we initially assume all postseismic deformation is the result of elastic deformation of the  
172 crust caused by slip occurring exclusively on the subduction interface. Cumulative  
173 displacements over the 2015-2016 period are not considered for inversion, as the  
174 magnitude of deformation is small and the data is limited (Figure 2b). *GTdef* [Chen et al.,  
175 2009] is used to perform an inversion of the 2012-2015 surface displacement vectors.

176 We perform a bounded, weighted linear least squares inversion, similar to previous  
177 Nicoya deformation studies [Feng et al., 2012; Protti et al., 2014; Kyriakopoulos and  
178 Newman, 2016]. For a subduction interface defined by coincident pair nodes, Green's  
179 functions are obtained for each node-station pair assuming unit slip on each patch. For  
180 surface displacement observations ( $d$ ) weighted ( $W$ ) by their errors ( $d' = Wd$ ), the  
181 weighted Green's functions ( $G' = WG$ ) are used to solve the linear system  $d' = G'm$  for

182 slip on the interface ( $\mathbf{m}$ ) [Jónsson et al., 2002; Feng et al., 2012; Kyriakopoulos &  
183 Newman, 2016].

184 Allowing hundreds of fault solutions with independent slips results in an  
185 underdetermined problem for the 120 observations available (40 stations, each with 3  
186 components). To allay this and avoid unrealistic variations in slip over small distances on  
187 the fault, the full inversion also applies smoothing conditions along strike and dip:  
188

$$189 \begin{bmatrix} \mathbf{d}' \\ \mathbf{0} \end{bmatrix} = \begin{bmatrix} \mathbf{G}' \\ \kappa^2 \mathbf{D} \end{bmatrix} \mathbf{m}$$

190  
191 which includes a Lagrangian smoothness weighting multiplier ( $\kappa$ ) and the second order  
192 Laplacian smoothing operator ( $\mathbf{D}$ ) [see Jónsson et al., 2002 for details]. In all cases, a  
193 Poisson's ratio of 0.25 is assumed over a range of  $\kappa$  values.

194 Generally model misfit increases with smoothing, resulting in a tradeoff between  
195 smoothness of the fault solution and residual error. This leads to a non-unique suite of  
196 results, dependent on  $\kappa$ , from which the preferred solution must be selected [e.g. Gubbins,  
197 2004]. Most commonly the inflection point in a curve of roughness ( $\rho$ ) versus root mean  
198 squared (RMS) misfit is subjectively chosen for a preferred solution, such that additional  
199 smoothing produces an unacceptably large increase in misfit [e.g. Jónsson et al., 2002;  
200 Chen et al., 2009]. Here:

$$201 \rho = \frac{\sum_i |\mathbf{p}_i|}{2N}$$

202 for  $\mathbf{p} = \mathbf{Dm}$  for each patch,  $i$ , for a total of  $N$  fault patches, and normally described in  
203  $\text{cm}/\text{km}^2$ .

204 The inversion is performed first with a simplified, 2D-curvilinear geometry  
205 consistent with Feng et al. [2012], and then with a detailed fully 3D model consistent  
206 with Kyriakopoulos and Newman [2016]. We implement high-resolution 3D fault  
207 geometry to better represent subduction heterogeneities like the East Pacific Rise-Cocos  
208 Nazca Spreading Center (EPR-CNS) transition (Figure 1) or potential subducted  
209 seamounts [e.g. Protti et al, 1995; Husen et al., 2002; Wang & Bilek, 2011]. Specifically,  
210 we use the slab surface of Kyriakopoulos et al. [2015], determined using the Maximum  
211 Seismicity Method described therein. This model, which represents the most recent,  
212 detailed characterization of the interface is superior in Nicoya where the main coseismic  
213 rupture area straddles crustal material of heterogeneous provenience [Barckhausen et al.,  
214 2001]. Due to the higher resolution of the 3D model, we leave details of the model  
215 based on the 2D geometry for the electronic supplement and Figure S1. We present the  
216 2D geometry to highlight that slip details are largely similar between geometries and are  
217 not substantially affected by complexity in the topographically diverse 3D interface of  
218 *Kyriakopoulos et al.* [2015]. Subsequent discussion will correspond to the 3D model and  
219 results.

220 As detailed in Kyriakopoulos & Newman [2016], the subduction surface is  
221 discretized into a Finite Element Model (FEM) with 43 along-strike by 21 along-dip  
222 coincident pair nodes, each patch having an area of approximately 5x5 km. Maximum  
223 depth varies between 36 km in the south and 67 km at the northern edge, resulting from  
224 an angle of subduction which is dramatically steeper in the northern EPR crust [Figure 6a  
225 in Kyriakopoulos et al., 2015]. Green's functions are subsequently calculated within FEM  
226 software, ABAQUS (<http://www.simulia.com/>). For the bounded least-squares inversion,

227 we allow up to 10 m of positive thrust or as strike-slip motion in either direction. These  
 228 slip limits are several times larger than expected (and ultimately modeled) postseismic  
 229 slip, and more than a factor of 2 greater than the maximum coseismic slip determined to  
 230 be about 4.4 m [Protti et al., 2014; Kyriakopoulos & Newman, 2016]. The edges of the  
 231 model are permitted to slip freely, except in ‘Fixed Surface’ inversions where slip is  
 232 forced to be zero at the trench. We view these two boundary conditions as end member  
 233 models, while noting that this model and network geometry are unable to resolve between  
 234 the two.

235 Spatial recoverability is limited by the distribution of GPS stations on the Nicoya  
 236 Peninsula. The spatial recoverability is evaluated by performing a checkerboard test using  
 237 an input grid with a cell size of 20x40 km, comparable to the size of features observed.  
 238 Starting with an initial model with alternating unit slip patches (1 m), split equally  
 239 between strike and dip slip components, we add white Gaussian noise corresponding to  
 240 the calculated GPS errors to the forward model prediction at each site. The resultant  
 241 displacements, plus error, are used as input for inversions that would ideally recover the  
 242 initial input checkerboard.

243 We also consider the model resolution matrix, used to quantify the area over  
 244 which individual model parameters affect one another [e.g. Gubbins, 2004]. The  
 245 resolution matrix,  $\mathbf{R} = \mathbf{G}^{-g}\mathbf{G}$  [Menke, 1989], is evaluated with the generalized inverse of  
 246 the weighted, damped least squares problem:  $\mathbf{G}^{-g} = (\mathbf{G}^T\mathbf{W}\mathbf{G} + \kappa\mathbf{D}^T\mathbf{D})^{-1}\mathbf{G}^T\mathbf{W}$  [Jónsson et  
 247 al., 2002; Kyriakopoulos & Newman, 2016]. If the inversion reproduced the true model  
 248 then  $\mathbf{R}$  would equal the identity matrix, but in practice the diagonals are somewhat less  
 249 than 1 with non-zero off-diagonal elements representing dependence between model  
 250 parameters [Gubbins, 2004]. The  $i$ -th row of the resulting resolution matrix provides a  
 251 measure of the tradeoff between that parameter and all other  $j$  parameters ( $j \neq i$ ), for a  
 252 specified smoothness weighting. A useful characterization of the resolution matrix is a  
 253 scalar field of the resolution spread parameter,  $r$ , described as:

254 
$$r_i = \frac{L_i}{\sqrt{R_i}}$$

255 for patch length  $L_i$  and diagonals of  $\mathbf{R}$  given by  $R_i$  [Funning et al., 2005]. This value,  $r_i$ , is  
 256 useful in visualizing the spatial interdependence of model parameters.

257 A comparison of our checkerboard testing and the resolution spread parameter is  
 258 shown in Figure 4. We assign ‘good’ recoverability where the original checkerboard  
 259 shape can be distinguished, as opposed to locations in which the checkerboard is smeared  
 260 beyond recognition. Beneath the 40 postseismic GPS sites at approximately 15-20 km  
 261 spacing on the Nicoya Peninsula there is excellent recoverability over the western coast  
 262 of the peninsula. Denoted by the thick purple line in Figure 4b, the maximum zone of  
 263 recoverability extends to within ~30 km of the trench and matches approximately with  
 264 the 25 km resolution contour. This line denotes the points at which parameters on one  
 265 patch have a tradeoff with parameters on patches in the surrounding 25 km. Any slip  
 266 outside of this region cannot be appropriately estimated with this dataset and smoothing.  
 267

## 268 **3 RESULTS & DISCUSSION**

### 269 **3.1 Surface Displacements**

270 For the period for which we have the most complete GPS coverage, 2012-2015,  
 271 GPS-determined horizontal surface displacements are primarily trenchward with offsets

272 between 7 and 26 cm. As described in Wang et al. [2012], we expect that afterslip will  
273 cause wholesale seaward motion, while viscoelastic relaxation should increasingly push  
274 coastal stations landward and inland stations seaward. Accordingly, any seaward motion  
275 of coastal sites is likely to be the result of afterslip rather than relaxation. Large seaward  
276 displacements near the coast suggest that afterslip is occurring, and at least in the shallow  
277 subduction zone, may be a dominant mechanism operating over this period.

278 Comparing velocities over the last year of observation (Table 2) to late  
279 interseismic velocities of 15-25 mm/yr NNE [Table 1 of Feng et al., 2012], we identify  
280 that a transition to pre-seismic convergence rates has not yet occurred. As megathrust  
281 coupling reinitiates we should again expect to observe a transition from seaward to  
282 landward surface velocities, that should eventually approximate the prior interseismic  
283 rates, with clear landward motion initiating at coastal sites and propagating inland [Wang,  
284 2012]. In contrast, the 2015-2016 period shows dominantly trench-parallel motion of 4-  
285 27 mm/yr NW. Convergence, though not yet returned to interseismic rates, suggests that  
286 afterslip is ceasing and that there are likely overlapping contributions from minor  
287 continued afterslip, early relocking, and viscoelastic relaxation to the observed surface  
288 deformation field.

289

### 290 **3.2 Afterslip Inversion**

291 We explored a range of  $\kappa$  values for this inversion (Figure 5), choosing the  
292 preferred  $\kappa$  value of 9000 near the inflection point in our models. This point is similar in  
293 both the freely-sliding and fixed surface models, because deviations in model results  
294 primarily occur in the near-trench environment where our data are insensitive to model  
295 variability; differences in parameters are outside of the area of recoverability. To  
296 demonstrate the effect of over- or undersmoothing, Figure 5 includes slip results for  $\kappa$  of  
297 4000 and 18000, inset top right. While the maximum amount of slip varies only slightly  
298 between these three models, the rougher solution contains several segments of slip in  
299 small patches while the smoother solution averages slip over large areas to produce a map  
300 with only three slipping patches. The two patches of slip on the seaward coast of the  
301 peninsula remain in all three cases and are considered robust. Only the preferred result  
302 will be discussed further. We compare our observed surface displacements with those  
303 predicted from the freely-sliding trench inversion (Figure 6). Generally, the horizontal  
304 displacements are well matched while the smaller vertical vectors are more variable.  
305 Results are similar for the fixed surface model (Figure S2).

306 Within the zone of recoverability, slip inversion results display a maximum of 1.7  
307 m of reverse slip. This is true of both the freely-slipping and fixed trench surface cases  
308 (Figures 7 and 8, respectively). Fixed and freely-slipping boundary conditions both have  
309 a cumulative postseismic slip moment ( $M_o$ ) of  $2.0 \times 10^{20}$  Nm ( $M_w$  7.5) inside the zone of  
310 recoverability, assuming rigidity of 30 GPa, with comparable RMS residuals (14.54 and  
311 14.56 mm; Figure 5). The primary difference between these cases lies outside of the zone  
312 of recoverability (denoted by thick purple line in Figures 7 and 8), with more shallow slip  
313 suggested by the freely-slipping trench case. While we do not have data sufficiently close  
314 to the trench to determine the existence of slip there, Davis et al. [2015] use pressure  
315 changes from the time of the mainshock until the end of 2013 to estimate up to 0.76 m of  
316 postseismic slip at the toe. We therefore consider these two results as end members, but  
317 prefer the freely-slipping (non-fixed) trench model (Figure 7).

318 Three patches of significant afterslip both up and downdip of the coseismic  
319 rupture area (pink contour) are imaged in Figures 7b and 8b. The strongest slip is near the  
320 coastline in two distinct patches at roughly 15-20 km depth on either side of the EPR-  
321 CNS transition, with some slip extending seaward along the transition. Downdip there is  
322 a diffuse zone of up to 0.7 m slip, running parallel to strike between roughly 25-50 km  
323 depth. Lastly, a region of slip is imaged in the south end of the zone of recoverability,  
324 beneath the Gulf of Nicoya, with a maximum of 0.9 m of slip at 15-40 km depth.

### 325 326 **3.3 Comparison to Aftershocks**

327 Afterslip is a response to unrelieved interseismic stress and any additional  
328 coseismically induced stresses that are commonly thought to at least partially drive  
329 aftershocks [e.g. Hsu et al., 2006; Chan & Stein, 2009; Helmstetter & Shaw, 2009]. If  
330 coseismic slip is assumed to drive postseismic behavior, then the occurrence of either  
331 aftershocks or afterslip is likely the result of differing frictional parameters on the fault  
332 surface. Afterslip is thought to be the preferred release mechanism for velocity-  
333 strengthening materials whereas aftershocks nucleate where the surface is velocity-  
334 weakening [e.g. Marone et al., 1991; Helmstetter & Shaw, 2009]. This hypothesis requires  
335 the observed postseismic behaviors to be spatially separated at any point in time. To  
336 explore the veracity of this idea in the current case, we compare our preferred afterslip  
337 model with the aftershock distribution of Yao et al. [2017]. This catalog contains 7747  
338 events over 4 months from the 5 September mainshock to the end of 2012, with local  
339 magnitudes ( $M_L$ ) up to 5.7 (corresponding to the largest  $M_w$  6.4 aftershock). To reduce  
340 noise associated with more poorly determined events, we evaluate a subset of the catalog  
341 with a minimum of 10 associated P and S wave arrivals, each, and a formal RMS error of  
342 less than the average plus one standard deviation. The resulting subset of 5381 events is  
343 plotted in Figures 7a and 8a, along with the repeating earthquakes of Yao et al. [2017].

344 Near the peninsula, the majority of aftershocks are concentrated in clusters  
345 immediately southeast of the EPR-CNS boundary near the “elbow” of the coastline and at  
346 the southern tip of the peninsula near Cabo Blanco Park. Notably both aftershock clusters  
347 have experienced episodic tremor prior to the 2012 earthquake [Walter et al., 2011].  
348 Areas of strong updip afterslip near the coastline are bounded laterally by aftershock  
349 clusters, with little aftershock activity in the regions of greatest afterslip. A similar anti-  
350 correlation of aftershocks and afterslip was previously observed for the 2004 Parkfield  
351 and 2005 Nias earthquake [Hsu et al., 2006], with the former being interpreted as the  
352 result of frictional properties that vary along strike [Barbot et al., 2009]. It is likely that  
353 the same is occurring at Nicoya over depths of 15-20 km where the anticorrelation is  
354 strongest. Almost all repeating earthquakes are located in this same depth range, although  
355 they also appear to be anticorrelated with strong afterslip. This is an unexpected finding,  
356 given that the current literature on repeating earthquakes suggests that they are commonly  
357 the result of small patches of slip-weakening material embedded within a broader slip-  
358 strengthening region [e.g. Nadeau & McEvilly, 1999; Beeler, Lockner & Hickman, 2001;  
359 Chen & Lapusta, 2009]. The notion that these repeaters are the result of surrounding  
360 aseismic slip has even been implemented by Uchida and Matsuzawa [2013] to use  
361 repeating aftershocks as a proxy for afterslip following the 2011  $M_w$  9.0 Tohoku-Oki  
362 earthquake. It appears, however, that this technique is not uniformly applicable to all  
363 small, repeating aftershocks.

364 Over the coseismic depth range of roughly 20-30 km we see more distributed  
365 aftershocks occurring, albeit with a lower density of events than immediately above. This  
366 is consistent with a sustained velocity-weakening behavior in the seismogenic zone over  
367 the postseismic period. The shallowest 10 km of the subduction interface also experiences  
368 diffuse but poorly located aftershocks, while in the 10-15 km and 30-50 km range there is  
369 little observed seismicity and only modest afterslip. Total moment from aftershocks is not  
370 calculated [Yao et al., 2017], but their contribution to slip is included in estimates herein.

371 Interseismic seismicity, as recorded by the CRSEIZE experiment [DeShon et al.,  
372 2006], is more dispersed along strike despite the majority of interplate events also  
373 locating between 15-20 km depth. This suggests that slip-strengthening behavior may be  
374 ephemeral at this depth, being initiated by the 2012 earthquake.  
375

### 376 **3.4 Comparison to Inter- and Coseismic Slip**

377 When examining the entire seismic cycle ‘slip budget’ on the subduction  
378 interface, it is crucial to consider the spatial relationship of locking, coseismic slip, and  
379 afterslip. In the along-dip direction, afterslip occurs both above and below the coseismic  
380 slip region, with maximum afterslip (1.7 m) nearly one-half of the observed coseismic  
381 slip (4 m) [Kyriakopoulos & Newman, 2016]. Likewise, the moment released by afterslip  
382 within the region of recoverability ( $M_o = 2.0 \times 10^{20}$  Nm,  $M_w$  7.5) is about one-half of that  
383 observed coseismically ( $M_o = 3.7 \times 10^{20}$  Nm,  $M_w$  7.6) [Kyriakopoulos & Newman, 2016].  
384 Following the 2012 earthquake, Protti et al. [2014] observed that a portion of the  
385 interseismically locked area just offshore remained unruptured during the mainshock  
386 (Figure 7b and 8b). While we observe that a large segment has slipped during the  
387 postseismic phase, a portion appears to remain locked. To quantify this, we estimate the  
388 spatial distribution of slip deficit since the most recent prior Nicoya megathrust  
389 earthquake.

390 Using the interseismic locking model of Kyriakopoulos & Newman [2016; based  
391 on Feng et al., 2012] and a constant convergence at 83 mm/yr [DeMets et al., 2010], the  
392 maximum accumulated slip from 1950-2012 in regions of 100% coupling is estimated to  
393 be 5.15 m. From this we subtract coseismic slip [Kyriakopoulos & Newman, 2016; based  
394 on Protti et al., 2014] and our preferred afterslip model. The total remaining moment at  
395 seismogenic depths between 10 and 30 km is  $M_o = 2.0 \times 10^{20}$  Nm ( $M_w$  7.5), and includes  
396 contributions from several patches (Figure 9). This value is likely an overestimate as it  
397 does not explicitly account for slip associated with intermediate sized earthquakes (e.g.  
398 1978, 1990), and assumes the late-interseismic locking as observed between about 2000  
399 and 2010 to be constant through the interseismic period. Furthermore, slow slip events,  
400 which are implicitly included if they occurred during the observed late-interseismic  
401 period, may too change over time. Beneath most of the peninsula, it appears that  
402 interseismic strain energy is largely relieved by coseismic and postseismic slip, with < 1  
403 m residuals. However, a large slip deficit (>3 m) remains within the southeastern edge of  
404 the zone of recoverability. This overlaps a region of frequent slow slip (discussed in  
405 following section) and the 1990  $M_w$  7.0 earthquake at the entrance to the Gulf of Nicoya  
406 [Protti et al., 1995], which likely accounts for some of the deficit reported here.

407 Directly beneath the elbow of the peninsula (Punto Guiones), the approximate  
408 transition between EPR and CNS crust and the location of intense aftershock seismicity,  
409 we find more than 2 m of slip deficit still remains. As an update from the Protti et al.

410 [2014] result, we find the patch of unresolved slip near Punto Guiones to have  $5.3 \times 10^{19}$   
411 Nm of unrecovered moment, capable of up to an  $M_w$  7.1 earthquake (indicated by pink  
412 polygon, Figure 9). While such an event certainly has an increased tsunami potential  
413 over the prior under-land rupture in 2012, we suspect it is unlikely to extend significantly  
414 toward the trench like the destructive 1992 Nicaragua tsunami earthquake that occurred  
415 immediately northwest of the Nicoya Peninsula [e.g. Kanamori & Kikuchi, 1993; Satake  
416 et al., 1993, Ihmlé, 1996]. The lack of significant seismogenic coupling in this region,  
417 supported by seafloor pressure data of Davis et al. [2015], suggests slip is being relieved  
418 aseismically near the trench.

419

### 420 **3.5 Comparison to Slow Slip**

421 The approximately 0.8 m of afterslip at the southernmost, downdip extent of the  
422 peninsula near the entrance to the Gulf of Nicoya, though possibly biased by the edge of  
423 the model, is intriguing. Nearby continuous GPS sites show a clear temporary reversal in  
424 very early 2014 and another potential event in 2015 (Figures 3, S3) – transient  
425 southwestward displacement consistent with the direction of coseismic, postseismic, and  
426 previous slow slip event (SSE) displacements. This location has experienced slow slip  
427 events in 2007, 2009, as well as in 2012 prior to and concurrent with the Nicoya  
428 earthquake [Dixon et al., 2014]. Voss et al. [2017] find up to 0.14 m slip in the Gulf of  
429 Nicoya area during the 2014 SSE, accounting for only 18% of the observed afterslip in  
430 the Gulf. This suggests that afterslip and SSE's are both occurring in this region, which  
431 may be associated with a subducting seamount that nucleated the 1990  $M_w$  7.0  
432 earthquake in the Gulf of Nicoya [Husen et al., 2003].

433 Frequent aseismic slips along the Nicoya margin may help relieve stored strain  
434 energy, and is likely tied to elevated fluid pressures. Extremely high  $V_p/V_s$  [Audet &  
435 Schwartz, 2013] and abruptly reduced seismic velocities following the 2012 mainshock  
436 [Chaves & Schwartz, 2016] indicate forearc pore pressures that may approach lithostatic,  
437 effectively weakening the upper plate and allowing slow slip events approximately every  
438 1-2 years unless loaded coseismically [Audet & Schwartz, 2013; Dixon et al., 2014].

439

### 440 **3.6 Potential Anelastic Contributions**

441 An elongate and diffuse region of up to 0.7 m of slip is observed near the downdip  
442 edge of the study region, with slip at depth greater than 30 km accounting for 22% of the  
443 total afterslip moment within the zone of recoverability. While our modeled slip may  
444 accurately represent elastic behavior of the subduction interface just downdip of  
445 coseismic slip, it is also likely that there is an appreciable anelastic contribution.  
446 Malservisi et al. [2015] found that the 2-year postseismic GPS time series across 18  
447 continuous stations on the peninsula are well fit by combined relaxation functions with  
448 characteristic timescales of 7, 70, and greater than 400 days, suggesting contributions  
449 from poroelastic deformation, afterslip, and downdip viscoelastic relaxation, respectively.  
450 We identify that this idea is supported by the paucity of aftershock activity below ~30 km  
451 depth (Figures 7b and 8b), although the CRSEIZE experiment recorded seismicity at  
452 these depths during the interseismic period [DeShon et al., 2006]. A detailed tomographic  
453 model, developed by DeShon et al., [2006], estimated that the Mohorovičić discontinuity  
454 intersects the slab at 30-40 km beneath Nicoya, updip of our observed deep afterslip.

455 Postseismic viscoelastic relaxation is expected following large megathrust events,  
456 though the relative proportions of relaxation and afterslip are difficult to determine due to  
457 their shared seaward motion of the upper plate [Wang et al., 2012]. Because the current  
458 model assumes all deformation is on-fault and elastic, we are similarly unable to resolve  
459 between deep fault slip and distributed relaxation of the upper mantle. Estimates herein of  
460 deep afterslip should therefore be taken as an end member behavior. Evaluating the  
461 anelastic component of postseismic deformation will become increasingly important  
462 when considering longer time periods leading toward relocking of the megathrust.  
463 Similarly, this model also makes no attempt to model poroelastic relaxation. While  
464 Malservisi et al. [2015] posit a short-period relaxation signal consistent with poroelastic  
465 effects, modeled displacements from poroelastic rebound were found to be significantly  
466 smaller than the displacements associated with that 7-day relaxation and directionally  
467 inconsistent with poroelastic stressing. We suspect that the poroelastic effect is likely to  
468 be only a modest contribution as compared to the dominant afterslip signal observed over  
469 the 2.5-year period.

470

### 471 **3.7 Spatially Variable Fault Behavior on the Nicoya Megathrust**

472 Synthesizing all of our observations about slip, there are substantial differences in  
473 afterslip along strike and dip. At the 15-20 km depth range along the entire Nicoya  
474 Peninsula, postseismic activity appears as either afterslip with little seismicity or as  
475 aftershock clusters with little observed cumulative slip. Given that this band experiences  
476 spatially similar loading by stress heterogeneities at the edge of the coseismic rupture  
477 area, such variable slip behavior along strike must be the result of changes in thermal,  
478 geological, frictional, and/or structural regime.

479 The thermal state of the Nicoya Peninsula is dominantly controlled by the change  
480 in provenance of the oceanic crust between relatively warm CNS and abnormally cold  
481 EPR material [Harris & Wang, 2002; Hutnak et al., 2007]. Afterslip and aftershocks  
482 nucleating at the same depth along the southern CNS crust, where temperatures should be  
483 fairly constant, suggests that the spatial separation of afterslip and aftershocks at the same  
484 depth is not significantly thermally controlled. Similarly, hanging wall lithology is  
485 consistent in the along-strike direction across the Nicoya Peninsula [Bourgeois et al.,  
486 1984] and subducting crusts are similar ages even across the EPR-CNS suture  
487 [Barckhausen et al., 2001]. This suggests no substantial age-related or lithologic control.

488 Rate-and-state friction dictates that when a sufficient stress is applied to a fault it  
489 will fail seismically or aseismically depending on whether the interface material is  
490 velocity-weakening or velocity-strengthening, respectively [e.g. Dieterich, 1972; Ruina,  
491 1983; Scholz, 1998]. If the subduction interface is velocity-weakening near Punto  
492 Guiones (elbow in coastline), it would resist slipping aseismically and instead nucleate  
493 aftershocks in a region surrounded by stress heterogeneities in the down dip and lateral  
494 directions. A similar contrast in frictional parameters in the along strike direction was  
495 previously observed by Barbot et al., [2009] for the 2004 Parkfield earthquake, where  
496 afterslip was anticorrelated with aftershocks, and explains the disconnected nature of  
497 afterslip patches near the coast.

498 Other than the clear transition in material origin and thermal state across the  
499 downgoing plate, the only other notable difference is the existence of ‘subducted  
500 topography’ along the interface associated with the CNS crust [Kyriakopoulos et al.,

501 2015]. As discussed in Yao et al., [2017], aftershock clusters occur along and possibly  
502 within the microseismically-defined indenters immediately south of the elbow in the  
503 coast (the focus of most coseismic rupture in 2012), as well as near the continuation of  
504 the Fisher Seamount chain subducting at the southernmost tip of the peninsula near Cabo  
505 Blanco (just north of the 1990 earthquake, indicated in Figure 1) [Kyriakopoulos et al.,  
506 2015]. Subducted seamounts, the most commonly discussed indenter, are often associated  
507 with abundant microseismicity and occasionally larger earthquakes with complex rupture  
508 patterns [Wang & Bilek, 2011]. In the current study, we note that coseismic slip and  
509 aftershock activity appears to terminate above approximately 20 km depth, except in  
510 zones of significant slab topography, suggesting that topography primarily affects the  
511 updip extent of aftershock behavior.

512

### 513 **3.8 Continuing Postseismic Deformation**

514 Visual inspection of continuous GPS time series shows the postseismic response  
515 curve has flattened for many sites (Figure 3), suggesting that afterslip and postseismic  
516 relaxation may be approaching completion by 2015 [e.g. Wang et al., 2012]. Continued  
517 observations are critical as the landward velocities increase toward interseismic values.  
518 This process may begin at the toe of the subduction zone and propagate inland, as is now  
519 observed in Chile following the 1960  $M_w$  9.5 Valdivia earthquake [Wang et al., 2007],  
520 rendering coastal observations particularly crucial for understanding the exact timing of  
521 relocking. This coastal initiation of landward motion is thought to be from superposition  
522 of both interseismic plate convergence and postseismic viscoelastic relaxation, which is  
523 expected to be landward at coastal stations and seaward at inland stations due to the  
524 opposing directions of relaxation between the oceanic mantle and mantle wedge [Wang et  
525 al., 2012]. Because stress-related postseismic processes largely overlap both temporally  
526 and spatially, including afterslip, aftershocks, poroelastic and viscoelastic relaxation, it is  
527 difficult to uniquely isolate their individual contributions, particularly when the time  
528 scales of some behaviors may be stress dependent [e.g. Bürgmann and Dresen 2008].  
529 This can become further complicated later in the postseismic cycle as portions of the  
530 interface begin to relock, while others still slip, and postseismic relaxation processes are  
531 ongoing—this is where we find Nicoya in 2015.

532 Keeping an updated budget of potential slip during the next megathrust event will  
533 improve seismic hazard assessments. Current GPS monument configuration may also  
534 prove useful for determining the spatiotemporal evolution of the early interseismic  
535 period, wherein the width of the locked seismogenic zone is expected to narrow as  
536 downdip frictional locking decreases [Wang & Tréhu, 2016]. Evaluating more complex  
537 models (e.g. viscoelastic and pore-pressure response, rate-and-state friction law) has  
538 improved our understanding of the crustal and mantle response to rapid coseismic loading  
539 [e.g. Jónsson et al., 2003; Barbot et al., 2009; Johnson et al., 2009; Hu et al., 2016].  
540 Given the ideal geometry and rich data across the Nicoya Peninsula, application of such  
541 models to this dataset should provide quantitative estimates of the mantle rheology and  
542 characteristic timescale of recovery for Nicoya, ideal for comparison with measurements  
543 of megathrusts worldwide.

544

545

546

547 **5 CONCLUSIONS**

548 Using three and a half years of dense GPS measurements following the 5  
549 September 2012  $M_w$  7.6 Nicoya Peninsula, Costa Rica earthquake, we identify distinct  
550 patterns spatial and temporal evolution of postseismic deformation. Strong seaward  
551 displacements occur over the first 2.5-year period and diminish to almost zero trench-  
552 normal velocities by mid-2016. This indicates relocking has initiated, but GPS velocities  
553 have yet to return to interseismic rates observed in the decade prior to the mainshock.

554 Modeled afterslip, using the 3D subduction interface model of Kyriakopoulos et  
555 al., [2015], found up to 1.7 m of motion in two slip patches immediately updip of  
556 coseismic rupture, below the western coast of the peninsula. Comparison with afterslip  
557 results from a model using the 2D geometry (Figure S1 and accompanying text) are  
558 similar with the 3D results presented herein, suggesting the observed slip distribution is  
559 not an artifact of complex model geometry. Aftershock seismicity occurs in two clusters:  
560 between these coastal afterslip patches and directly southeast of the southern patch,  
561 forming a 15-20 km deep band of strong postseismic activity running the entire length of  
562 the peninsula. Differences in behavior along this band may be tied to varying frictional  
563 properties and/or the distribution of subducted topography. A region of deeper slip  
564 imaged at the downdip edge of coseismic rupture may be real or could be the result of  
565 unmodeled viscoelastic relaxation. At the southeast edge of the study area, near the Gulf  
566 of Nicoya, another patch of significant afterslip exists near the locus of several slow slip  
567 events. One such event in 2014 is thought to account for less than 20% of the cumulative  
568 slip in this region, thus significant afterslip is still required to explain most deformation.

569 Ultimately, afterslip and aftershocks are spatially distinct, and primarily outline  
570 the updip edge of the 2012 coseismic rupture. While some aftershocks are seen to be  
571 repeating [Yao *et al.*, 2017], the spatial distribution of aftershock behavior is insufficient  
572 to describe the afterslip signal.

573 Future measurements with this network will provide insights about the relocking  
574 and early interseismic behavior along this megathrust. Such details are useful for  
575 comparison with other subduction zones without such favorable land geometry, as well as  
576 for estimation of seismic and tsunami hazard in Costa Rica as the Nicoya megathrust  
577 enters another seismic cycle.

578

579 **Acknowledgements:**

580 NSF funding to AVN through 1447104 and 1262267. NSERC funding to TEH through  
581 PGSD2-488063-2016. Raw continuous and campaign GPS are available at  
582 UNAVCO.org. Model outputs are available at <http://nicoya.eas.gatech.edu>. Fieldwork  
583 would not have been possible without the help of B. Burgoa, K. Gardner, M. Kemmerlin,  
584 A. Williamson, and J. McAdams. We thank T. Dixon for valuable input in shaping this  
585 manuscript, as well as thorough reviews from J. Hsu and three anonymous reviewers.

586 **References:**

587

588 Altamimi, Z., Collilieux, X., & Métivier, L. (2011). ITRF2008: an improved solution of  
589 the international terrestrial reference frame. *Journal of Geodesy*, 85(8), 457-473.

590 Audet, P., & Schwartz, S. Y. (2013). Hydrologic control of forearc strength and  
591 seismicity in the Costa Rican subduction zone. *Nature Geoscience*, 6(10), 852-855.

592 Barbot, S., Fialko, Y., & Bock, Y. (2009). Postseismic deformation due to the Mw 6.0  
593 2004 Parkfield earthquake: Stress-driven creep on a fault with spatially variable rate-  
594 and-state friction parameters. *Journal of Geophysical Research: Solid Earth*, 114(B7).

595 Barckhausen, U., Ranero, C. R., Huene, R. V., Cande, S. C., & Roeser, H. A. (2001).  
596 Revised tectonic boundaries in the Cocos Plate off Costa Rica: Implications for the  
597 segmentation of the convergent margin and for plate tectonic models. *Journal of*  
598 *Geophysical Research: Solid Earth*, 106(B9), 19207-19220.

599 Beeler, N. M., Lockner, D. L., & Hickman, S. H. (2001). A simple stick-slip and creep-  
600 slip model for repeating earthquakes and its implication for microearthquakes at  
601 Parkfield. *Bulletin of the Seismological Society of America*, 91(6), 1797-1804.

602 Blewitt, G. (2008). Fixed point theorems of GPS carrier phase ambiguity resolution and  
603 their application to massive network processing: Ambizap. *Journal of Geophysical*  
604 *Research: Solid Earth*, 113(B12).

605 Bourgois, J., Azema, J., Baumgartner, P. O., Tournon, J., Desmet, A., & Aubouin, J.  
606 (1984). The geologic history of the Caribbean-Cocos Plate boundary with special  
607 reference to the Nicoya ophiolite complex (Costa Rica) and DSDP results (Legs 67  
608 and 84 off Guatemala): A synthesis. *Tectonophysics*, 108(1-2), 1-32.

609 Bürgmann, R., & G. Dresen (2008). Rheology of the lower crust and upper mantle:  
610 Evidence from rock mechanics, geodesy, and field observations. *Annu. Rev. Earth*  
611 *Planet. Sci.*, 36, 531-567, doi: [10.1146/annurev.earth.36.031207.124326](https://doi.org/10.1146/annurev.earth.36.031207.124326)

612 Chan, C. H., & Stein, R. S. (2009). Stress evolution following the 1999 Chi-Chi, Taiwan,  
613 earthquake: consequences for afterslip, relaxation, aftershocks and departures from  
614 Omori decay. *Geophysical Journal International*, 177(1), 179-192.

615 Chaves, E. J., & Schwartz, S. Y. (2016). Monitoring transient changes within  
616 overpressured regions of subduction zones using ambient seismic noise. *Science*  
617 *Advances*, 2(1), e1501289.

618 Chen, T., & Lapusta, N. (2009). Scaling of small repeating earthquakes explained by  
619 interaction of seismic and aseismic slip in a rate and state fault model. *Journal of*  
620 *Geophysical Research: Solid Earth*, 114(B1).

621 Chen, T., Newman, A. V., Feng, L., & Fritz, H. M. (2009). Slip distribution from the 1  
622 April 2007 Solomon Islands earthquake: A unique image of near-trench  
623 rupture. *Geophysical Research Letters*, 36(16).

624 Davis, E. E., Villinger, H., & Sun, T. (2015). Slow and delayed deformation and uplift of  
625 the outermost subduction prism following ETS and seismogenic slip events beneath  
626 Nicoya Peninsula, Costa Rica. *Earth and Planetary Science Letters*, 410, 117-127.

- 627 DeMets, C., Gordon, R. G., & Argus, D. F. (2010). Geologically current plate  
628 motions. *Geophysical Journal International*, *181*(1), 1-80.
- 629 DeShon, H. R., Schwartz, S. Y., Newman, A. V., González, V., Protti, M., Dorman, L.  
630 M., Dixon, T., Sampson, D.E., & Flueh, E. R. (2006). Seismogenic zone structure  
631 beneath the Nicoya Peninsula, Costa Rica, from three-dimensional local earthquake P-  
632 and S-wave tomography. *Geophysical Journal International*, *164*(1), 109-124.
- 633 Dieterich, J. H. (1972). Time-dependent friction in rocks. *Journal of Geophysical*  
634 *Research*, *77*(20), 3690-3697.
- 635 Dinc, A. N., Koulakov, I., Thorwart, M., Rabbel, W., Flueh, E. R., Arroyo, I., Taylor, W.,  
636 & Alvarado, G. (2010). Local earthquake tomography of central Costa Rica: transition  
637 from seamount to ridge subduction. *Geophysical Journal International*, *183*(1), 286-  
638 302.
- 639 Dixon, T. H., Jiang, Y., Malservisi, R., McCaffrey, R., Voss, N., Protti, M., & Gonzalez,  
640 V. (2014). Earthquake and tsunami forecasts: Relation of slow slip events to  
641 subsequent earthquake rupture. *Proceedings of the National Academy of*  
642 *Sciences*, *111*(48), 17039-17044.
- 643 Ekström, G., Nettles, M., & Dziewoński, A. M. (2012). The global CMT project 2004–  
644 2010: centroid-moment tensors for 13,017 earthquakes. *Physics of the Earth and*  
645 *Planetary Interiors*, *200*, 1-9.
- 646 Estey, L. H., & Meertens, C. M. (1999). TEQC: the multi-purpose toolkit for  
647 GPS/GLONASS data. *GPS solutions*, *3*(1), 42-49.
- 648 Feng, L., Newman, A. V., Protti, M., Gonzalez, V., Jiang, Y., & Dixon, T. H. (2012).  
649 Active deformation near the Nicoya Peninsula, northwestern Costa Rica, between  
650 1996 and 2010: Interseismic megathrust coupling. *Journal of Geophysical Research:*  
651 *Solid Earth*, *117*(B6).
- 652 Gubbins, D. (2004). *Time series analysis and inverse theory for geophysicists*. Cambridge  
653 University Press.
- 654 Harris, R. N., & Wang, K. (2002). Thermal models of the middle America trench at the  
655 Nicoya Peninsula, Costa Rica. *Geophysical Research Letters*, *29*(21).
- 656 Harris, R. N., Spinelli, G., Ranero, C. R., Grevemeyer, I., Villinger, H., & Barckhausen,  
657 U. (2010). Thermal regime of the Costa Rican convergent margin: 2. Thermal models  
658 of the shallow Middle America subduction zone offshore Costa Rica. *Geochemistry,*  
659 *Geophysics, Geosystems*, *11*(12).
- 660 Helmstetter, A., & Shaw, B. E. (2009). Afterslip and aftershocks in the rate-and-state  
661 friction law. *Journal of Geophysical Research: Solid Earth*, *114*(B1).
- 662 Hsu, Y. J., Simons, M., Avouac, J. P., Galetzka, J., Sieh, K., Chlieh, M., ... & Bock, Y.  
663 (2006). Frictional afterslip following the 2005 Nias-Simeulue earthquake,  
664 Sumatra. *Science*, *312*(5782), 1921-1926.

665 Hu, Y., Wang, K., He, J., Klotz, J., & Khazaradze, G. (2004). Three-dimensional  
666 viscoelastic finite element model for postseismic deformation of the great 1960 Chile  
667 earthquake. *Journal of Geophysical Research: Solid Earth*, 109(B12).

668 Hu, Y., Bürgmann, R., Uchida, N., Banerjee, P., & Freymueller, J. T. (2016). Stress-  
669 driven relaxation of heterogeneous upper mantle and time-dependent afterslip  
670 following the 2011 Tohoku earthquake. *Journal of Geophysical Research: Solid  
671 Earth*, 121(1), 385-411.

672 Husen, S., Kissling, E., & Quintero, R. (2002). Tomographic evidence for a subducted  
673 seamount beneath the Gulf of Nicoya, Costa Rica: The cause of the 1990 Mw= 7.0  
674 Gulf of Nicoya earthquake. *Geophysical Research Letters*, 29(8).

675 Hutnak, M., Fisher, A. T., Stein, C. A., Harris, R., Wang, K., Silver, E., Spinelli, G.,  
676 Pfender, M., Villinger, H., MacKnight, R. & Pisani, P. C. (2007). The thermal state of  
677 18–24 Ma upper lithosphere subducting below the Nicoya Peninsula, northern Costa  
678 Rica margin. *The Seismogenic Zone of Subduction Thrust Faults*, 86-122.

679 Ihmlé, P. F. (1996). Monte Carlo slip inversion in the frequency domain:: Application to  
680 the 1992 Nicaragua Slow Earthquake. *Geophysical research letters*, 23(9), 913-916.

681 International Seismological Centre, *On-line Bulletin*, <http://www.isc.ac.uk>, Internatl.  
682 Seismol. Cent., Thatcham, United Kingdom, 2014.

683 Jiang, Y., Wdowinski, S., Dixon, T. H., Hackl, M., Protti, M., & Gonzalez, V. (2012).  
684 Slow slip events in Costa Rica detected by continuous GPS observations, 2002–  
685 2011. *Geochemistry, Geophysics, Geosystems*, 13(4).

686 Johnson, K. M., Bürgmann, R., & Freymueller, J. T. (2009). Coupled afterslip and  
687 viscoelastic flow following the 2002 Denali Fault, Alaska earthquake. *Geophysical  
688 Journal International*, 176(3), 670-682.

689 Jónsson, S., Segall, P., Pedersen, R., & Björnsson, G. (2003). Post-earthquake ground  
690 movements correlated to pore-pressure transients. *Nature*, 424(6945), 179-183.

691 Jónsson, S., Zebker, H., Segall, P., & Amelung, F. (2002). Fault slip distribution of the  
692 1999 Mw 7.1 Hector Mine, California, earthquake, estimated from satellite radar and  
693 GPS measurements. *Bulletin of the Seismological Society of America*, 92(4), 1377-  
694 1389.

695 Kanamori, H., & Kikuchi, M. (1993). The 1992 Nicaragua earthquake: a slow tsunami  
696 earthquake. *Nature*, 361, 25.

697 Khazaradze, G., Wang, K., Klotz, J., Hu, Y., & He, J. (2002). Prolonged post-seismic  
698 deformation of the 1960 great Chile earthquake and implications for mantle  
699 rheology. *Geophysical Research Letters*, 29(22).

700 Kyriakopoulos, C., Newman, A. V., Thomas, A. M., Moore-Driskell, M., & Farmer, G.  
701 T. (2015). A new seismically constrained subduction interface model for Central  
702 America. *Journal of Geophysical Research: Solid Earth*, 120(8), 5535-5548.

- 703 Kyriakopoulos, C., & Newman, A. V. (2016). Structural asperity focusing locking and  
704 earthquake slip along the Nicoya megathrust, Costa Rica. *Journal of Geophysical*  
705 *Research: Solid Earth*, 121, doi:10.1002/2016JB012886.
- 706 LaFemina, P., Dixon, T. H., Govers, R., Norabuena, E., Turner, H., Saballos, A., Mattioli,  
707 G., Protti, M., & Strauch, W. (2009). Fore-arc motion and Cocos Ridge collision in  
708 Central America. *Geochemistry, Geophysics, Geosystems*, 10(5).
- 709 Letellier, T. (2005). *Etude des ondes de marée sur les plateaux continentaux* (Doctoral  
710 dissertation, Toulouse 3).
- 711 Liu, C., Zheng, Y., Xiong, X., Wang, R., López, A., & Li, J. (2015). Rupture processes of  
712 the 2012 September 5 Mw 7.6 Nicoya, Costa Rica earthquake constrained by  
713 improved geodetic and seismological observations. *Geophysical Journal*  
714 *International*, 203(1), 175-183.
- 715 Malservisi, R., Schwartz, S. Y., Voss, N., Protti, M., Gonzalez, V., Dixon, T. H., Jiang,  
716 Y., Newman, A.V., Richardson, J., Walter, J.I., & Voyenko, D. (2015). Multiscale  
717 postseismic behavior on a megathrust: The 2012 Nicoya earthquake, Costa  
718 Rica. *Geochemistry, Geophysics, Geosystems*, 16(6), 1848-1864.
- 719 Marone, C. J., Scholtz, C. H., & Bilham, R. (1991). On the mechanics of earthquake  
720 afterslip. *Journal of Geophysical Research: Solid Earth*, 96(B5), 8441-8452.
- 721 Marshall, J. S., & Anderson, R. S. (1995). Quaternary uplift and seismic cycle  
722 deformation, Peninsula de Nicoya, Costa Rica. *Geological Society of America*  
723 *Bulletin*, 107(4), 463-473.
- 724 Menke, W. (1989). *Geophysical Data Analysis: Discrete Inverse Theory* (revised ed.)  
725 Academic Press. *San Diego*.
- 726 Nadeau, R. M., & McEvilly, T. V. (1999). Fault slip rates at depth from recurrence  
727 intervals of repeating microearthquakes. *Science*, 285(5428), 718-721.
- 728 Newman, A. V., Schwartz, S. Y., Gonzalez, V., DeShon, H. R., Protti, J. M., & Dorman,  
729 L. M. (2002). Along-strike variability in the seismogenic zone below Nicoya  
730 Peninsula, Costa Rica. *Geophysical Research Letters*, 29(20).
- 731 Outerbridge, K. C., Dixon, T. H., Schwartz, S. Y., Walter, J. I., Protti, M., Gonzalez, V.,  
732 Biggs, J., Thorwart, M., & Rabbel, W. (2010). A tremor and slip event on the Cocos-  
733 Caribbean subduction zone as measured by a global positioning system (GPS) and  
734 seismic network on the Nicoya Peninsula, Costa Rica. *Journal of Geophysical*  
735 *Research: Solid Earth*, 115(B10).
- 736 Protti, M., McNally, K., Pacheco, J., Gonzalez, V., Montero, C., Segura, J., Brenes, J.,  
737 Barboza, V., Malavassi, E., Güendel, F., & Simila, G. (1995). The March 25, 1990  
738 (Mw= 7.0, ML= 6.8), earthquake at the entrance of the Nicoya Gulf, Costa Rica: Its  
739 prior activity, foreshocks, aftershocks, and triggered seismicity. *Journal of*  
740 *Geophysical Research: Solid Earth*, 100(B10), 20345-20358.
- 741 Protti, M., González, V., Newman, A. V., Dixon, T. H., Schwartz, S. Y., Marshall, J. S.,  
742 Feng, L., Walter, J.I., Malservisi, R., & Owen, S. E. (2014). Nicoya earthquake

- 743 rupture anticipated by geodetic measurement of the locked plate interface. *Nature*  
744 *Geoscience*, 7(2), 117-121.
- 745 Ruina, A. (1983). Slip instability and state variable friction laws. *Journal of Geophysical*  
746 *Research: Solid Earth*, 88(B12), 10359-10370.
- 747 Sak, P. B., Fisher, D. M., Gardner, T. W., Marshall, J. S., & LaFemina, P. C. (2009).  
748 Rough crust subduction, forearc kinematics, and Quaternary uplift rates, Costa Rican  
749 segment of the Middle American Trench. *Geological Society of America*  
750 *Bulletin*, 121(7/8), 992-1012.
- 751 Satake, K., Bourgeois, J., Abe, K., Abe, K., Tsuji, Y., Imamura, F., ... & Estrada, F.  
752 (1993). Tsunami field survey of the 1992 Nicaragua earthquake. *EOS*  
753 *Transactions*, 74(13), 145-157.
- 754 Scholz, C. H. (1998). Earthquakes and friction laws. *Nature*, 391(6662), 37-42.
- 755 Vannucchi, P., Scholl, D. W., Meschede, M., & McDougall-Reid, K. (2001). Tectonic  
756 erosion and consequent collapse of the Pacific margin of Costa Rica: Combined  
757 implications from ODP Leg 170, seismic offshore data, and regional geology of the  
758 Nicoya Peninsula. *Tectonics*, 20(5), 649-668.
- 759 Voss, N., Dixon, T., Liu, Z., Malservisi, R., Schwartz, S.Y., Protti, M. & Gonzalez, V.  
760 (2016). Post earthquake slow slip following the 2012 Nicoya Earthquake. *AGU*  
761 *Chapman Conference on the Slow Slip Phenomena*.
- 762 Walter, J. I., Schwartz, S. Y., Protti, J. M., & Gonzalez, V. (2011). Persistent tremor  
763 within the northern Costa Rica seismogenic zone. *Geophysical Research*  
764 *Letters*, 38(1).
- 765 Walter, J. I., Schwartz, S. Y., Protti, M., & Gonzalez, V. (2013). The synchronous  
766 occurrence of shallow tremor and very low frequency earthquakes offshore of the  
767 Nicoya Peninsula, Costa Rica. *Geophysical Research Letters*, 40(8), 1517-1522.
- 768 Walter, J. I., Meng, X., Peng, Z., Schwartz, S. Y., Newman, A. V., & Protti, M. (2015).  
769 Far-field triggering of foreshocks near the nucleation zone of the 5 September 2012  
770 (M W 7.6) Nicoya Peninsula, Costa Rica earthquake. *Earth and Planetary Science*  
771 *Letters*, 431, 75-86.
- 772 Wang, K., Hu, Y., Bevis, M., Kendrick, E., Smalley, R., Vargas, R. B., & Lauría, E.  
773 (2007). Crustal motion in the zone of the 1960 Chile earthquake: Detangling  
774 earthquake-cycle deformation and forearc-sliver translation. *Geochemistry,*  
775 *Geophysics, Geosystems*, 8(10).
- 776 Wang, K., & Bilek, S. L. (2011). Do subducting seamounts generate or stop large  
777 earthquakes?. *Geology*, 39(9), 819-822.
- 778 Wang, K., Hu, Y., & He, J. (2012). Deformation cycles of subduction earthquakes in a  
779 viscoelastic Earth. *Nature*, 484(7394), 327-332.
- 780 Wang, K., & Tréhu, A. M. (2016). Invited review paper: Some outstanding issues in the  
781 study of great megathrust earthquakes—The Cascadia example. *Journal of*  
782 *Geodynamics*, 98, 1-18.

783 Yao, D., Walter, J.I., Meng, X., Hobbs, T.E., Peng, Z., Newman, A.V., Schwartz, S.Y.,  
784 and Protti, M. (2017). Detailed Spatio-Temporal Evolution of Microseismicity and  
785 Repeating Earthquakes following the 2012  $M_w$ 7.6 Nicoya Earthquake. *Journal of*  
786 *Geophysical Research: Solid Earth*, 121, doi:10.1002/2016JB013632.

787 Yue, H., Lay, T., Schwartz, S. Y., Rivera, L., Protti, M., Dixon, T. H., Owen, S., &  
788 Newman, A. V. (2013). The 5 September 2012 Nicoya, Costa Rica Mw 7.6 earthquake  
789 rupture process from joint inversion of high-rate GPS, strong-motion, and teleseismic  
790 P wave data and its relationship to adjacent plate boundary interface  
791 properties. *Journal of Geophysical Research: Solid Earth*, 118(10), 5453-5466.

792

793

794 **Table 1:** Displacements and errors from 2012-2015 at Campaign and Continuous GPS

795 stations used in this study. Dates in decimal years, displacements relative to stable

796 Caribbean plate.

Station	Longitude	Latitude	Elev. [m]	Start	End	E [mm]	eE [mm]	N [mm]	eN [mm]	U [mm]	eU [mm]
<b>Campaign</b>											
BAG A	-85.261	10.5414	123.49	2012.7022	2015.1945	-53.87	5.06	-51.08	3.91	-37.67	19.07
BALL	-85.448	10.3834	118.03	2012.7077	2015.1836	-67.01	3.54	-71.98	2.85	50.80	12.19
BON G	-85.207	9.7438	21.54	2012.6940	2015.1945	-82.47	2.75	-112.97	2.18	-7.01	9.79
CEBA	-85.776	10.2491	90.43	2012.6967	2015.1863	-84.13	2.78	-140.81	2.54	1.28	11.16
COBA	-85.107	9.6881	172.44	2012.7240	2015.1890	-55.06	6.08	-52.37	5.08	-15.35	26.49
DIRI	-85.611	10.2718	82.04	2012.6940	2015.1781	-123.10	3.47	-143.86	2.72	35.10	11.81
GRAN	-85.653	10.5622	122.24	2012.7022	2015.1890	-59.94	2.84	-56.37	2.34	14.25	9.72
GUA2	-85.450	10.1401	136.32	2012.6913	2015.1781	-117.24	3.34	-169.28	2.81	-20.76	12.53
GUIO	-85.659	9.9231	31.42	2012.6913	2015.1808	-117.78	2.97	-198.44	2.47	120.61	10.35
HOJA	-85.382	10.0795	240.97	2012.6858	2015.1808	-128.77	3.57	-173.65	3.36	-17.86	14.84
JICA	-85.136	9.9751	61.40	2012.6995	2015.1863	-85.65	3.11	-99.23	2.44	23.58	10.97
LEON	-85.187	9.9365	276.91	2012.6885	2015.1836	-127.69	3.09	-124.48	2.55	20.31	10.78
MATA	-85.813	10.3553	77.82	2012.6967	2015.2000	-77.63	7.96	-91.02	7.73	22.22	40.87
MIRM	-85.571	10.0421	433.75	2012.7158	2015.1890	-98.85	3.10	-160.09	2.55	-84.69	10.54
PALO	-85.220	10.2415	40.05	2012.7022	2015.1836	-55.40	2.92	-79.54	2.33	-25.66	10.77
PAQU	-84.955	9.8322	80.26	2012.7049	2015.1918	-53.02	3.21	-43.76	2.63	45.06	11.02
POTR	-85.569	10.8474	155.76	2012.7131	2015.1945	-25.89	2.98	-33.78	2.43	35.07	12.96
SAM A	-85.549	9.8892	45.91	2012.6913	2015.1781	-118.93	3.66	-161.10	3.00	54.37	13.21
SJOS	-84.948	10.3656	1062.14	2012.6995	2015.2000	-63.25	3.28	-39.97	2.68	-0.01	11.14
SJUA	-85.757	10.0632	44.58	2012.7104	2015.1863	-88.38	3.55	-155.78	2.66	76.04	13.12
TENO	-85.098	10.6018	373.35	2012.7131	2015.2055	-66.88	3.24	-44.32	2.73	25.94	11.75
VENA	-85.792	10.1611	24.98	2012.6940	2015.1863	-88.42	3.28	-147.66	2.55	38.94	11.36
<b>Continuous</b>											
BIJA	-84.577	9.7500	555.54	2012.7240	2015.1945	-10.67	2.68	7.40	2.19	24.37	10.27
BON2	-85.203	9.7645	28.33	2012.7049	2015.1945	-82.46	2.71	-99.36	2.31	24.24	9.95
CABA	-85.344	10.2379	26.78	2012.6803	2015.1945	-100.13	2.21	-125.06	1.81	73.06	7.72
ELVI	-85.446	10.3947	81.76	2012.7131	2015.1945	-75.29	2.09	-67.71	1.73	52.46	7.13
EPZA	-85.568	10.1409	668.60	2012.6803	2015.5671	-154.62	2.37	-205.49	1.79	-22.13	7.90
GRZA	-85.636	9.9155	39.69	2012.6967	2015.1945	-112.42	2.53	-181.98	2.00	111.81	8.79
HATI	-85.710	10.2922	58.69	2012.6803	2015.1945	-119.69	2.95	-171.40	2.27	11.24	9.91
HUA2	-85.352	10.0177	594.20	2012.6831	2015.1945	-150.02	2.53	-181.89	1.99	3.94	8.64
IND1	-85.502	9.8646	75.44	2012.6858	2015.1945	-140.75	2.86	-177.53	2.23	84.93	11.09
LAFE	-84.960	9.8071	65.17	2012.6803	2015.1945	-67.42	2.29	-69.41	1.97	70.43	10.32
LEPA	-85.031	9.9454	20.97	2012.7077	2015.1945	-65.70	2.47	-60.85	2.07	38.80	8.74

LMN L	-85.053	10.2675	102.85	2012.6803	2015.1945	-76.01	2.09	-73.74	1.69	44.52	7.07
PNE2	-85.829	10.1952	19.66	2012.7049	2015.1945	-77.53	3.01	-126.03	2.28	36.17	11.01
PUJE	-85.273	10.1140	29.10	2012.6803	2015.6411	-119.52	2.23	-141.66	1.79	55.46	7.54
PUM O	-84.967	10.0645	17.90	2012.6803	2015.1945	-69.20	2.23	-71.35	1.82	55.56	8.45
QSEC	-85.357	9.8404	17.74	2012.6803	2015.1945	-145.74	2.22	-178.47	1.75	42.87	7.70
SAJU	-85.711	10.0671	73.82	2012.6803	2015.1945	-112.18	2.23	-206.19	1.81	45.58	7.91
VERA	-84.869	10.8536	64.30	2012.6803	2015.1945	-39.70	2.53	-55.49	2.10	20.99	9.49

797

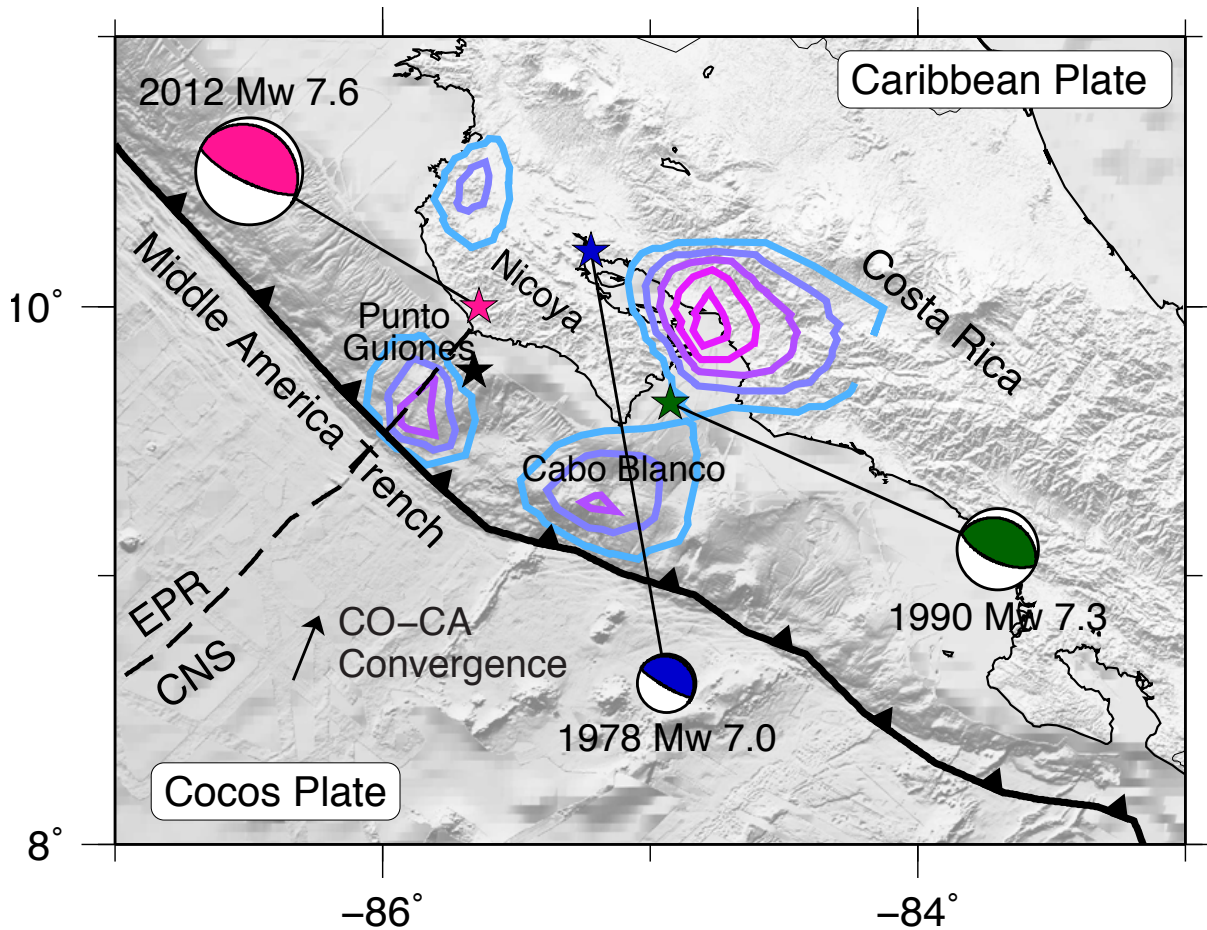
798 **Table 2:** Displacements and errors from 2015-2016 at Campaign and Continuous GPS

799 stations used in this study. Dates in decimal years, displacements relative to stable

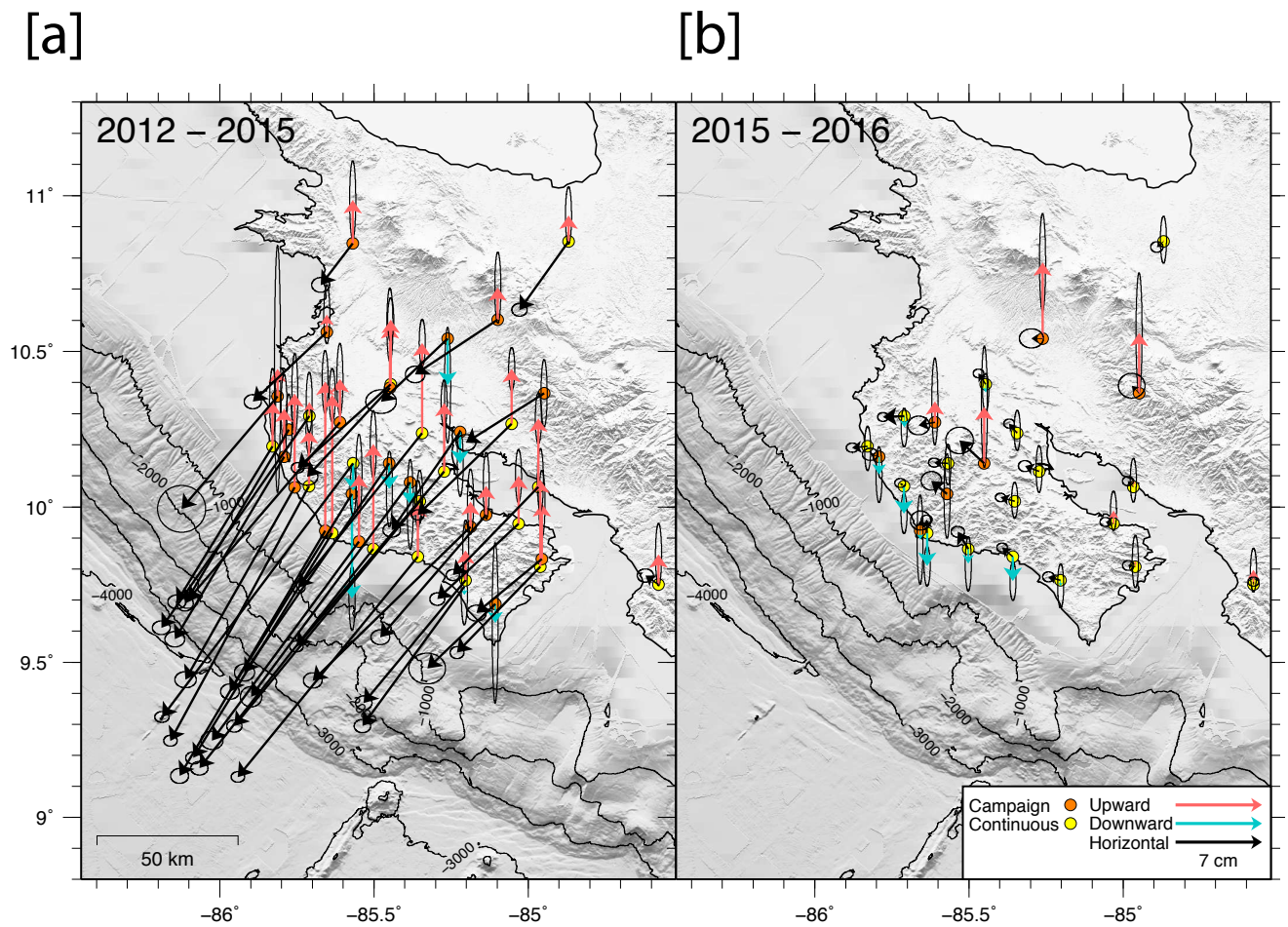
800 Caribbean plate.

Station	Longitude	Latitude	Elevation [m]	Start	End	E [mm]	eE [mm]	N [mm]	eN [mm]	U [mm]	eU [mm]
<b>Campaign</b>											
BAG A	-85.261	10.541	123.49	2015.186	2016.180	-9.02	3.97	0.12	3.16	61.84	16.12
DIRI	-85.611	10.272	82.04	2015.175	2016.175	-13.13	3.61	-2.45	3.09	16.96	14.36
GUA2	-85.450	10.140	136.32	2015.175	2016.169	-20.03	4.58	18.59	4.38	45.92	20.08
GUIO	-85.659	9.923	31.42	2015.178	2016.169	0.35	3.35	8.36	3.16	-7.11	14.72
MIRM	-85.571	10.042	433.75	2015.175	2016.169	-12.63	3.40	10.56	3.06	-1.66	14.01
SJOS	-84.948	10.366	1062.14	2015.197	2016.178	-5.97	4.40	6.10	4.10	48.91	19.89
VENA	-85.792	10.161	24.98	2015.184	2016.175	-7.12	2.60	2.04	1.99	-14.32	9.20
<b>Continuous</b>											
BIJA	-84.577	9.750	555.54	2015.175	2016.178	-0.08	1.81	2.42	1.51	11.76	7.21
BON2	-85.203	9.765	28.33	2015.175	2016.178	-9.85	1.90	2.63	1.65	-4.71	7.29
CABA	-85.344	10.238	26.78	2015.175	2016.178	-6.46	1.76	7.57	1.51	2.09	6.64
ELVI	-85.446	10.395	81.77	2015.175	2016.178	-5.83	1.74	8.75	1.44	-6.44	6.21
EPZA	-85.568	10.141	668.59	2015.559	2016.178	-11.16	1.88	0.44	1.47	-1.22	6.66
GRZA	-85.636	9.916	39.69	2015.175	2016.178	-0.40	1.81	11.06	1.44	-26.81	6.49
HATI	-85.710	10.292	58.68	2015.175	2016.178	-17.17	1.76	-0.74	1.46	-9.20	6.38
HUA2	-85.352	10.018	594.20	2015.175	2016.178	-11.47	1.69	3.25	1.39	1.07	5.92
IND1	-85.502	9.865	75.14	2015.175	2016.178	-8.45	2.22	13.93	1.79	-12.04	8.97
LAFE	-84.960	9.807	65.18	2015.175	2016.178	-5.74	1.86	1.18	1.64	4.30	8.68
LEPA	-85.031	9.945	20.97	2015.175	2016.178	-6.54	1.77	1.59	1.51	10.57	6.51
PNE2	-85.829	10.195	19.66	2015.175	2016.178	-12.39	2.00	-1.17	1.52	-1.73	7.34
PUJE	-85.273	10.114	29.09	2015.175	2016.178	-11.38	2.18	4.41	1.81	2.01	7.75
PUM O	-84.967	10.065	17.91	2015.175	2016.178	-4.40	1.81	4.70	1.51	5.43	7.20
QSEC	-85.357	9.840	17.73	2015.175	2016.178	-8.73	1.77	7.35	1.42	-19.89	6.38
SAJU	-85.711	10.067	73.81	2015.175	2016.178	-3.09	1.80	2.48	1.49	-22.21	6.64
VERA	-84.869	10.854	64.31	2015.175	2016.178	-5.35	2.04	-4.64	1.75	1.29	7.78

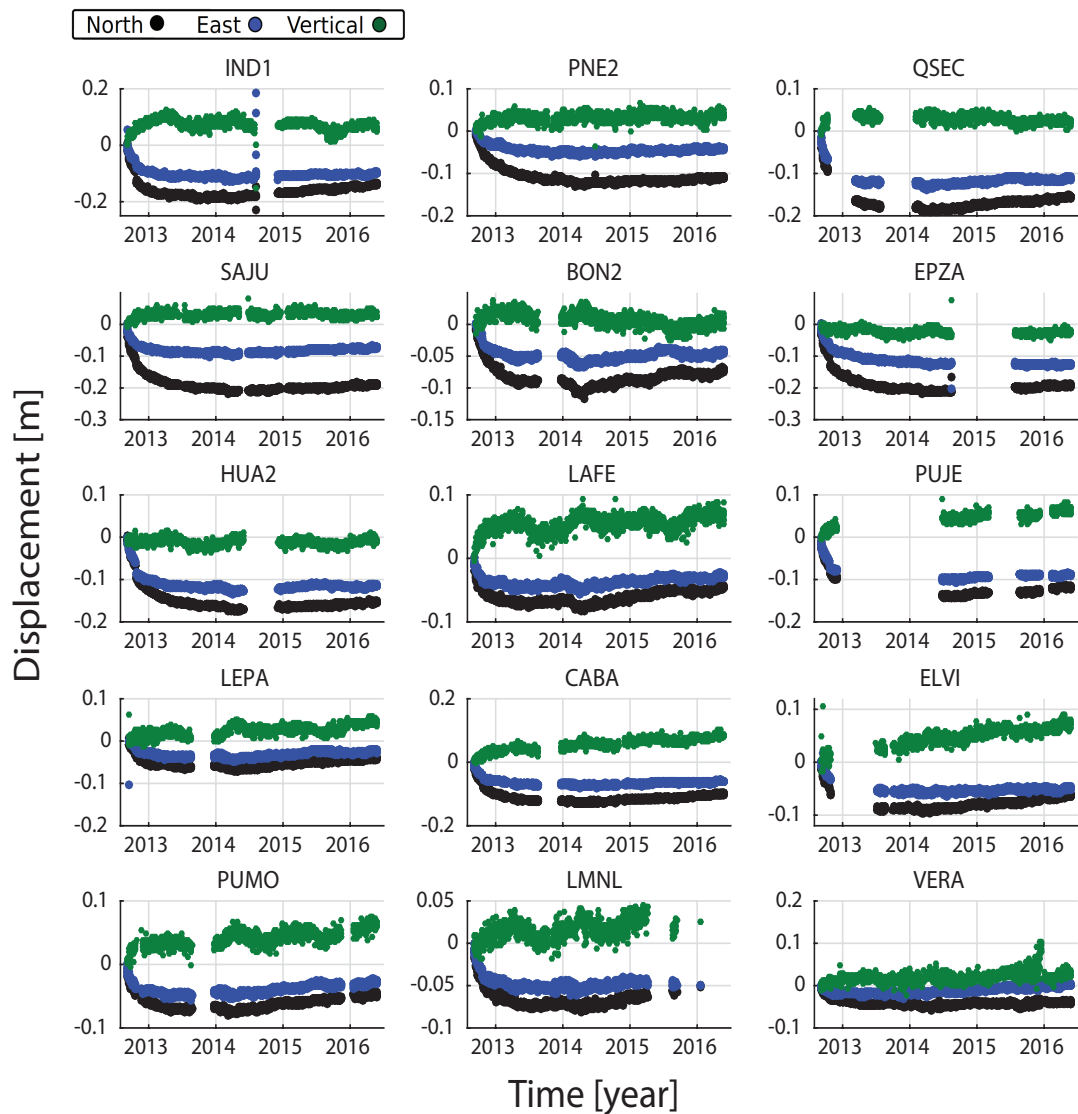
801



802  
 803 **Figure 1:** Tectonic configuration of Nicoya study area, with Cocos Plate subducting  
 804 beneath Caribbean Plate along the Middle America Trench in azimuth shown at a rate of  
 805 7.7 cm per year [DeMets et al., 2010]. Transition is shown from oceanic crust sourced at  
 806 the East Pacific Rise (EPR) and Cocos-Nazca Spreading Center (CNS) [Barckhausen et  
 807 al., 2001]. At this location there is a transition from steep subduction of relatively cold  
 808 EPR crust to the more shallowly downgoing and warmer CNS crust. Slow slip contours  
 809 of Dixon et al., [2014] shown from blue to pink in 100 cm intervals. Centroid [Ekström et  
 810 al., 2012] and relocated hypocenter [Yue et al., 2013] for 2012  $M_w$  7.6 Nicoya earthquake  
 811 shown by pink and black stars, respectively. The 1990  $M_w$  7.0 Gulf of Nicoya earthquake  
 812 [Protti et al., 1995] shown in green, and 1978  $M_w$  7.0 Samara earthquake [International  
 813 Seismological Centre] shown in blue. Global centroid-moment tensor solutions [Ekström  
 814 et al., 2012] shown by beachballs, scaled by magnitude. Fisher Seamount Chain can be  
 815 seen from bathymetry beneath the word ‘convergence’, heading toward the southern tip  
 816 of the Nicoya peninsula.  
 817

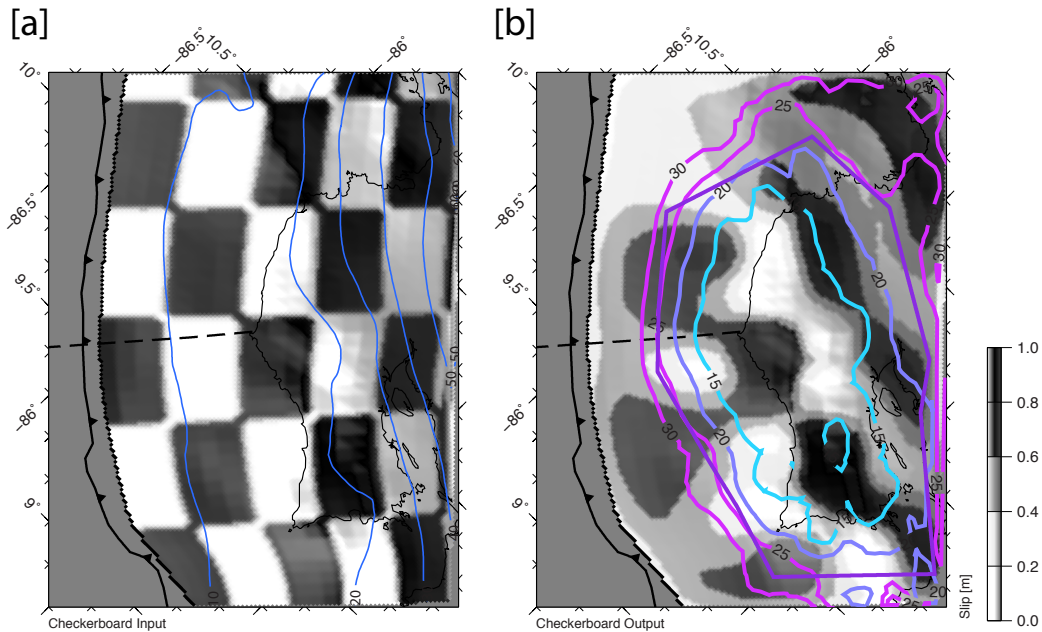


818  
 819 **Figure 2:** Displacement, relative to Caribbean plate, at campaign (orange) and continuous  
 820 (yellow) GPS sites for 2012-2015 (a) and 2015-2016 (b). Horizontal displacements in  
 821 black, upwards in red, and downwards in blue. Shown are the 22 available campaign  
 822 measurements from 2012-2015, compared to only 7 campaign sites successfully occupied  
 823 in 2016.  
 824  
 825



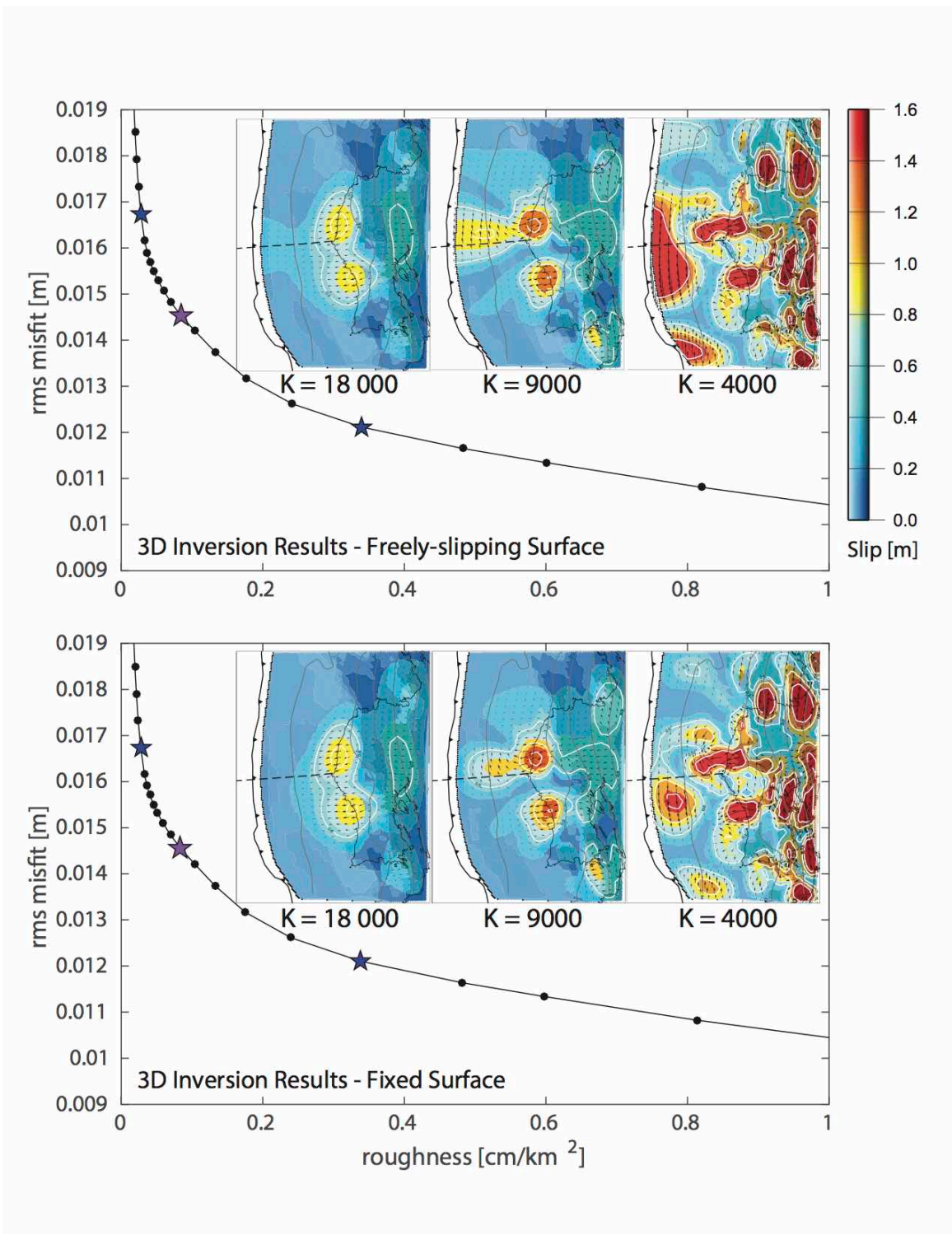
826  
 827  
 828  
 829  
 830  
 831  
 832  
 833  
 834  
 835  
 836

**Figure 3:** Displacement [meters] relative to the first day after the 2012 earthquake for a subset of continuous GPS stations having good temporal coverage. All offsets are given for a fixed Caribbean reference frame. Stations are arranged (left to right, starting from top row and working down) by distance from the trench. North, east, and vertical components are displayed in black, blue, and green, respectively. Postseismic daily displacements are large at first, diminishing with time, and ultimately reversing by approximately the start of 2015. Potential SSE's are visible as short-term reversals in direction of motion.

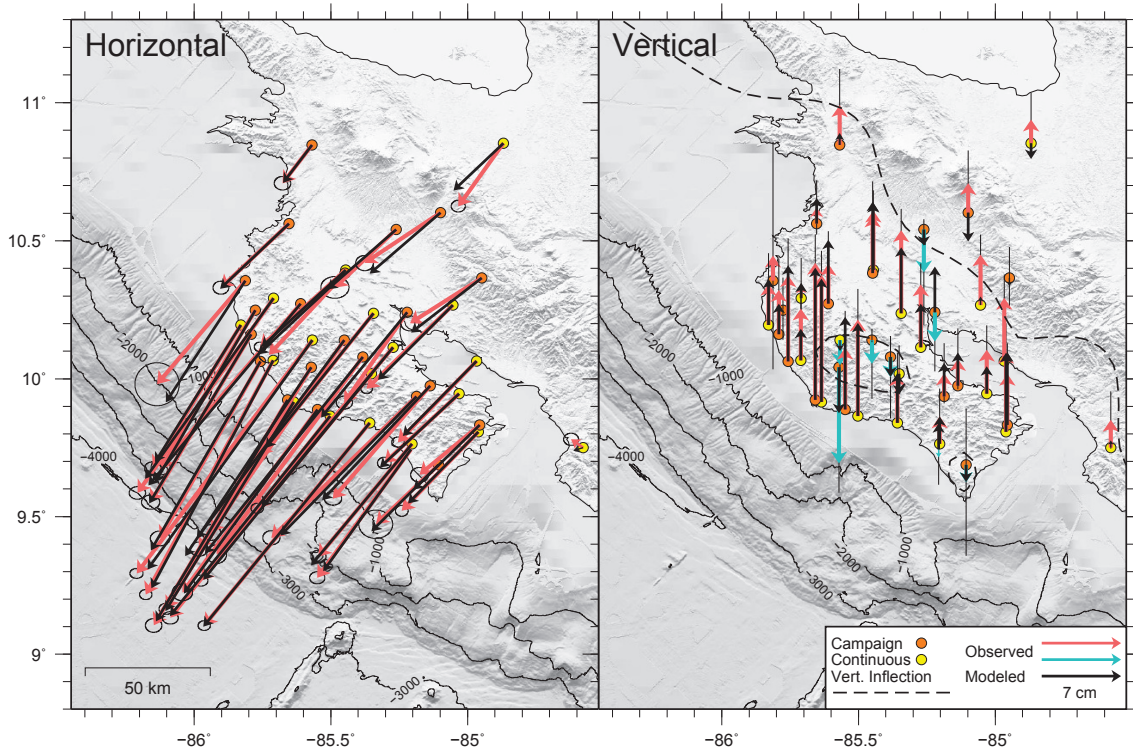


837  
 838  
 839  
 840  
 841  
 842  
 843  
 844  
 845  
 846

**Figure 4:** Results of checkerboard recoverability testing for input model (a) and resultant slip (b) using preferred smoothing value ( $\kappa = 9000$ ). Depth contours are overlain in blue over input slip panel. Output slip panel shows annotated contours of resolvability (in km) as well as a dark purple, angular polygon surrounding area for which there is good recoverability based on checkerboard test. For more information about resolution and recoverability tests please see Section 2.2. EPR-CNS suture shown as dashed line, MAT as solid line with teeth.

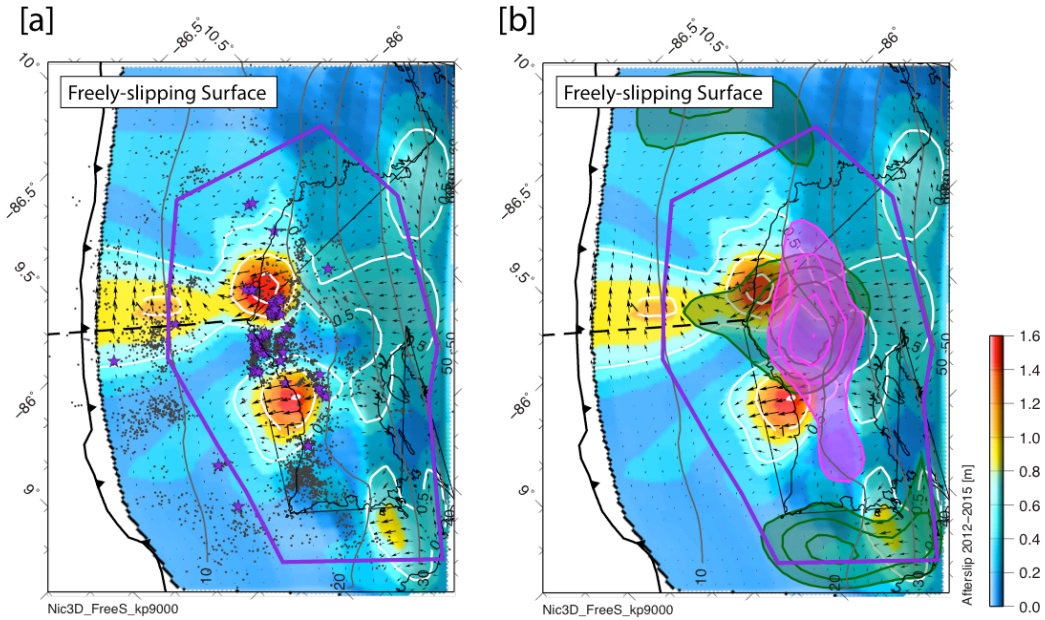


847  
 848 **Figure 5:** Roughness versus misfit for inversion of 2012-2015 GPS displacements.  
 849 Preferred solution of  $\kappa = 9000$  indicated by purple star. Blue stars indicate under- and  
 850 oversmoothed solutions of  $\kappa = 4000$  and  $18000$ . Resulting maps of afterslip are shown as  
 851 insets. From left to right they represent oversmoothed, preferred, and undersmoothed  
 852 results.  
 853

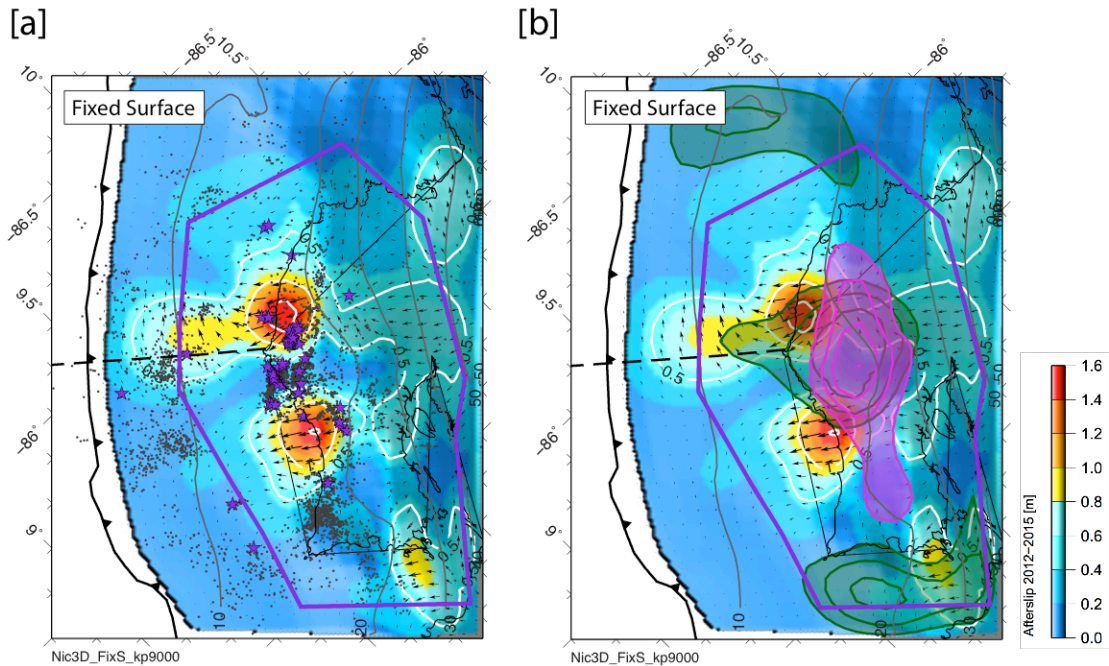


854  
 855 **Figure 6:** GPS displacements for 2012-2015 time period, shown for comparison against  
 856 model predictions for preferred slip result with free surface. Observations shown by  
 857 colored arrows, with predictions indicated by black arrows. Left panel shows horizontal  
 858 displacement, right shows vertical. Dashed line in right panel shows modeled zero  
 859 vertical deformation, separating uplift from subsidence.  
 860

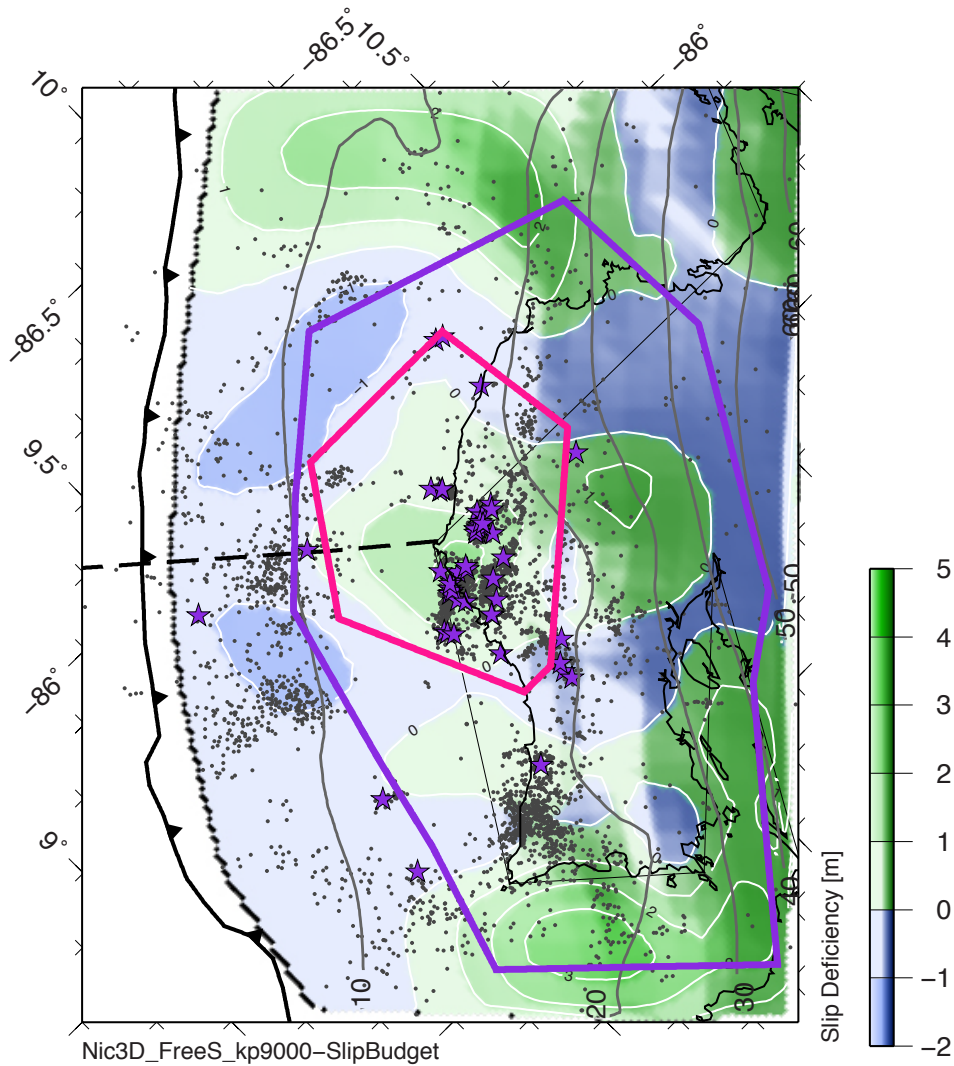
861  
862



863  
864 **Figure 7:** Both panels show result of 2012-2015 inversion where slip is allowed at the  
865 trench (non-fixed surface). Magnitude of total postseismic slip on the subduction  
866 interface is scaled by color, with arrows showing direction of hanging wall motion at  
867 each patch. White lines show 50 cm contours of slip. Thick black line with teeth marks  
868 the Middle America Trench, while thin grey lines show depth in 10 km intervals  
869 [Kyriakopoulos et al., 2015]. Dashed line shows EPR-CNS transition [Barckhausen et al.,  
870 2001]. Purple polygon denotes zone of recoverability, outside of which we are unable to  
871 resolve structures uniquely. (a) Aftershocks until end of 2012 shown as grey dots, with  
872 purple stars representing locations of repeating aftershock clusters [Yao et al., 2017]. (b)  
873 2012 coseismic slip contours shown in pink (every 100 cm), with percentage of pre-2012  
874 locking annotated and shown in green (20% intervals, starting at 50%) [Kyriakopoulos &  
875 Newman, 2016].  
876



878  
 879 **Figure 8:** Same as for Figure 7, except with inversion not allowing slip to rupture the  
 880 trench (fixed surface). Again, slip on the subduction interface is scaled by color, with  
 881 arrows showing direction of hanging wall motion at each patch. White lines show 50 cm  
 882 contours of slip. Purple polygon denotes zone of recoverability, outside of which we are  
 883 unable to resolve structures uniquely. (a) Aftershocks until end of 2012 shown as grey  
 884 dots, with purple stars representing locations of repeating aftershock clusters [Yao et al.,  
 885 2017]. (b) 2012 coseismic slip contours shown in pink (every 100 cm), with percentage  
 886 of pre-2012 locking annotated and shown in green (20% intervals, starting at 50%)  
 887 [Kyriakopoulos & Newman, 2016].  
 888



890

891

892 **Figure 9:** Slip deficit as difference between interseismic locking, coseismic slip, and  
 893 afterslip. Interseismic slip accumulation is calculated as percentage of interseismic  
 894 locking [Kyriakopoulos & Newman, 2016] multiplied by the full tectonic convergence  
 895 rate over 62 years. Afterslip is from non-fixed surface model. Negative slip deficit  
 896 represents slip overshoot. Overlain are aftershocks and repeating events from Figure 6a  
 897 and 7a [Yao et al., 2017]. Pink polygon shows the region of significant stored strain near  
 898 the elbow in the coastline, as discussed in Section 3.4. Purple polygon shows area of  
 899 recoverability, dashed black line is EPR-CNS transition from Barckhausen et al. [2001],  
 900 and thick black line with teeth marks the Middle America Trench.